

# More Synergies from Beauty, Top, $Z$ and Drell-Yan Measurements in SMEFT

Cornelius Grunwald,<sup>1,\*</sup> Gudrun Hiller,<sup>1,2,†</sup> Kevin Kröninger,<sup>1,‡</sup> and Lara Nollen<sup>1,§</sup>

<sup>1</sup>*TU Dortmund University, Department of Physics,  
Otto-Hahn-Str.4, D-44221 Dortmund, Germany*

<sup>2</sup>*Department of Physics and Astronomy, University of Sussex,  
Falmer, Brighton, BN1 9QH, United Kingdom*

We perform a global analysis of Beauty, Top,  $Z$  and Drell-Yan measurements in the framework of the Standard Model effective theory (SMEFT). We work within the minimal flavor violation (MFV) hypothesis, which relates different sectors and generations beyond the  $SU(2)_L$ -link between left-handed top and beauty quarks. We find that the constraints on the SMEFT Wilson coefficients from the combined analysis are stronger than the constraints from a fit to the individual sectors, highlighting synergies in the global approach. We also show that constraints within MFV are strengthened compared to single-generation fits. The strongest bounds are obtained for the semileptonic four-fermion triplet operator  $C_{lq}^{(3)}$ , probing scales as high as 18 TeV, followed by the gluon dipole operator  $C_{uG}$  with 7 TeV, and other four-fermion and penguin operators in the multi-TeV range. Operators with left-handed quark bilinears receive order one contributions from higher orders in the MFV expansion induced by the top Yukawa coupling as a result of the FCNC  $b \rightarrow s\mu\mu$  anomalies combined with the other sectors. We predict the 68% credible intervals of the dineutrino branching ratios within MFV as  $4.25 \cdot 10^{-6} \leq \mathcal{B}(B^0 \rightarrow K^{*0}\nu\bar{\nu}) \leq 11.13 \cdot 10^{-6}$  and  $2.26 \cdot 10^{-6} \leq \mathcal{B}(B^+ \rightarrow K^+\nu\bar{\nu}) \leq 5.78 \cdot 10^{-6}$ , which include the respective Standard Model predictions, and are in reach of the Belle II experiment. We show how future measurements of the dineutrino branching ratios can provide insights into the structure of new physics in the global fit.

## I. INTRODUCTION

The Standard Model (SM) continues to rule as the theory of the strong, weak and electromagnetic interactions, despite its shortcomings in addressing various observations and puzzles, including the origin of neutrino masses, the matter-antimatter asymmetry, flavor and dark matter, and the

\*Electronic address: cornelius.grunwald@tu-dortmund.de

†Electronic address: ghiller@physik.uni-dortmund.de

‡Electronic address: kevin.kroeninger@cern.ch

§Electronic address: lara.nollen@tu-dortmund.de

persisting tension with the  $b \rightarrow s\mu\mu$ -data. This implies that new physics (NP) is very weakly coupled, or the scale of physics beyond the Standard Model (BSM) is considerably larger than the scale of electroweak symmetry breaking. If such a separation of scales exist, a powerful tool to describe the low-energy effects of possible BSM physics are effective field theories (EFTs). In this regard, the Standard Model effective theory (SMEFT) has become increasingly important for phenomenology by delivering a framework to globally analyze data from various experiments, energies, and flavor sectors. In other words, SMEFT allows to "join forces" of the high energy and precision frontiers and therefore intensifies the search for NP. As SMEFT respects the  $SU(3)_C \times SU(2)_L \times U(1)_Y$ -symmetry, it directly links fermion flavors within weak isospin multiplets, notably top- and  $b$ -quarks, [1–4], but also different generations due to mixing [5, 6], as well as charged leptons and neutrinos. The latter as a means to test lepton flavor structures, such as universality or lepton flavor conservation, has been systematically explored recently in [7].

The number of SMEFT operators in the Warsaw basis [8] at dimensions six, 59, is large, and goes up to 2499 once fermion flavor structure is taken into account. Even though only a subset of operators contributes to a given process, including those via renormalization group mixing, the number of independent Wilson coefficients is in general too large for a fully model-independent analysis.

Flavor patterns linking various components of a given Wilson coefficient help here in two ways: different sectors, flavor changing neutral currents (FCNCs), charged currents and flavor diagonal observables, become correlated and thus can be combined in one global analysis, and the number of degrees of freedom in the global fit is reduced. Several flavor patterns have been considered in the literature, such as minimal flavor violation (MFV) [9–12], the top-philic approach [13, 14] or  $U(2)$  or  $U(3)$  symmetries [15–17].

Here we employ MFV to explore flavorful synergies within SMEFT, building upon and extending existing works [13], which was based on the top-philic approach. Previous SMEFT fits based on MFV do not include top observables [11], or focus on four-quark operators, including top [10] and dijet searches [12]. For earlier works, see [1, 18]. None of these works include LHC Drell-Yan data, which are powerful for flavor analyses and semileptonic four-fermion operators [19–22]. Our goal is to fill this gap and combine  $b \rightarrow s$  FCNCs, top,  $Z$  and Drell Yan measurements.

This paper is organized as follows: The effective field theory setup is introduced in Sec. II. The flavor structure of the Wilson coefficients based on MFV is given in Sec. III. In Sec. IV, we discuss the computation of observables and the sensitivities to the Wilson coefficients. Details of the fitting procedure and the results of the fit are presented in Sec. V, as well as the interplay with  $b \rightarrow s\nu\bar{\nu}$  branching ratios. We conclude in Sec. VI. Auxiliary information is provided in appendices

VIIA-VIIC.

## II. EFFECTIVE FIELD THEORY FRAMEWORKS

We briefly review SMEFT in Sec. IIA and give the operators and Wilson coefficients that contribute to the processes considered in this analysis. In Sec. IIB, we review the weak effective theory that is used to evaluate  $B$  physics observables.

### A. Standard Model Effective Field Theory

The SMEFT Lagrangian can be written as [23]

$$\mathcal{L}_{\text{SMEFT}} = \mathcal{L}_{\text{SM}} + \sum_{d=5}^{\infty} \sum_i \frac{C_i^{(d)}}{\Lambda^{d-4}} O_i^{(d)},$$

where  $O_i^{(d)}$  are operators of mass dimension  $d \geq 5$  composed out of SM fields,  $C_i^{(d)}$  are the corresponding Wilson coefficients and  $\Lambda$  denotes the scale of NP, which is assumed to be sufficiently above the electroweak scale governed by the vacuum expectation value of the Higgs,  $v = 246$  GeV.  $\mathcal{L}_{\text{SM}}$  stands for the Lagrangian of the SM. Odd-dimensional operators violate lepton or baryon number [24]. As we only consider processes that conserve these quantum numbers, we neglect such operators, hence also those with the lowest dimension,  $d = 5$ . We consider operators with dimension six, and drop in the following the corresponding superscript from operators and coefficients.

We employ the Warsaw basis [8], a non-redundant basis of dimension-six operators. Wilson coefficients carry in general quark and lepton flavor indices, inflating the number of operators. To relate different processes and reduce the degrees of freedom, we assume MFV. We discuss the flavor structure in detail in Sec. III. We restrict the Wilson coefficients to be real-valued, implying that we allow for no CP violation from beyond the SM. In our analysis, we consider the following operators:

$$\begin{aligned} O_{uG} &= (\bar{q}_L \sigma^{\mu\nu} T^A u_R) \tilde{\varphi} G_{\mu\nu}^A, & O_{uW} &= (\bar{q}_L \sigma^{\mu\nu} u_R) \tau^I \tilde{\varphi} W_{\mu\nu}^I, & O_{uB} &= (\bar{q}_L \sigma^{\mu\nu} u_R) \tilde{\varphi} B_{\mu\nu}, \\ O_{qe} &= (\bar{q}_L \gamma_\mu q_L) (\bar{e}_R \gamma^\mu e_R), & O_{lq}^{(1)} &= (\bar{l}_L \gamma_\mu l_L) (\bar{q}_L \gamma^\mu q_L), & O_{lq}^{(3)} &= (\bar{l}_L \gamma_\mu \tau^I l_L) (\bar{q}_L \gamma^\mu \tau^I q_L), \\ O_{eu} &= (\bar{e}_R \gamma_\mu e_R) (\bar{u}_R \gamma^\mu u_R), & O_{ed} &= (\bar{e}_R \gamma_\mu e_R) (\bar{d}_R \gamma^\mu d_R), & O_{lu} &= (\bar{l}_L \gamma_\mu l_L) (\bar{u}_R \gamma^\mu u_R), \\ O_{ld} &= (\bar{l}_L \gamma_\mu l_L) (\bar{d}_R \gamma^\mu d_R), & O_{\varphi q}^{(1)} &= (\varphi^\dagger i \overleftrightarrow{D}_\mu \varphi) (\bar{q}_L \gamma^\mu q_L), & O_{\varphi q}^{(3)} &= (\varphi^\dagger i \overleftrightarrow{D}_\mu^I \varphi) (\bar{q}_L \tau^I \gamma^\mu q_L), \\ O_{\varphi u} &= (\varphi^\dagger i \overleftrightarrow{D}_\mu \varphi) (\bar{u}_R \gamma^\mu u_R), & O_{\varphi d} &= (\varphi^\dagger i \overleftrightarrow{D}_\mu \varphi) (\bar{d}_R \gamma^\mu d_R). \end{aligned} \tag{1}$$

Here,  $q_L$  and  $l_L$  denote the left-handed  $SU(2)_L$  quark and lepton doublets,  $u_R$  and  $d_R$  the right-handed  $SU(2)_L$  up-type and down-type quark singlets and  $e_R$  the right-handed charged leptons. Each fermion field further carries a flavor index, which is suppressed here for brevity. The gauge field strength tensors of  $SU(3)_C$ ,  $SU(2)_L$  and  $U(1)_Y$  are denoted by  $G_{\mu\nu}^A$ ,  $W_{\mu\nu}^I$  and  $B_{\mu\nu}$ , respectively, with  $A = 1, \dots, 8$  and  $I = 1, 2, 3$ .  $T^A = \lambda^A/2$  and  $\tau^I/2$  are the generators of  $SU(3)_C$  and  $SU(2)_L$  in the fundamental representation, with the Gell-Mann matrices  $\lambda^A$  and the Pauli matrices  $\tau^I$ . We denote by  $\varphi$  the Higgs field and by  $\tilde{\varphi} = i\tau^2\varphi^*$  its conjugate. The covariant derivative is defined as  $D_\mu = \partial_\mu + ig'yB_\mu + i\frac{g}{2}\tau^I W_\mu^I + ig_s G_\mu^A T^A$  with the hypercharge  $y$ , gauge couplings  $g'$ ,  $g$  and  $g_s$  of  $U(1)_Y$ ,  $SU(2)_L$  and  $SU(3)_C$ , respectively, and the corresponding gauge fields  $B_\mu$ ,  $W_\mu^I$  and  $G_\mu^A$ . We further use  $\overleftrightarrow{D}_\mu = D_\mu - \overleftarrow{D}_\mu$  and  $\overleftrightarrow{D}_\mu^I = \tau^I D_\mu - \overleftarrow{D}_\mu \tau^I$ , and  $\varphi^\dagger \overleftrightarrow{D}_\mu \varphi = (D_\mu \varphi)^\dagger \varphi$ . The operators  $O_{uG}$ ,  $O_{uW}$  and  $O_{uB}$  are called (up-type quark) dipole operators, and the ones of type  $O_{\varphi x}$ ,  $x = u, d, q$  penguins, whereas the remaining ones in (1) are semileptonic four-fermion operators.

Further dimension-six operators beyond those given in (1) could contribute to the observables considered in this analysis. However, many of these are suppressed in MFV by lepton Yukawa couplings, or down-type quark Yukawas, which we neglect in our analysis, as detailed in Sec. III. This concerns, for instance, four-fermion tensor operators  $O_{ledq}$  and  $O_{lequ}^{(1,3)}$ , down-type quark and leptonic dipole operators. Furthermore, we neglect leptonic penguins, which are strongly constrained in purely leptonic transitions [18]. Moreover, we also neglect possible shifts of the SM couplings from bosonic operators after the diagonalization of the mass matrices [25].

The Wilson coefficients evolve with energy scale governed by the renormalization group equations (RGEs). These are computed at the one-loop level for the SMEFT [26–28]. For the numerical computation of the running, we employ the python package `wilson` [29]. We note that through RG-running operators in addition to (1) are induced such as four-quark or four-lepton operators. Those contributions are neglected in this work as the RG-induced effects are at most of the order of a few percent. We recall that MFV is radiatively stable [30], so RG-effects cannot switch on operators beyond MFV.

## B. Matching onto the Weak Effective Theory

While NP contributions to collider observables such as top-quark and Drell-Yan production can be described by SMEFT, the energy scale of  $b$ -hadron observables is considerably lower, below the electroweak scale. The appropriate theory in this region is the Weak Effective Theory (WET), in which the  $W, Z, h$  bosons as well as the top quark have been integrated out, and the SM gauge

symmetry is broken to  $SU(3)_C \times U(1)_{\text{em}}$ . For  $b \rightarrow s$  decays, the effective Lagrangian reads

$$\mathcal{L}_{\text{WET}}^{bs} = \frac{4G_F}{\sqrt{2}} V_{ts}^* V_{tb} \sum_i C_i(\mu) Q_i(\mu) \quad (2)$$

with Fermi's constant  $G_F = 1/(\sqrt{2}v^2)$ ,  $V_{ij}$  are elements of the Cabibbo Kobayashi Maskawa (CKM) matrix, and the effective operators

$$\begin{aligned} Q_7 &= \frac{e}{16\pi^2} m_b (\bar{s}_L \sigma^{\mu\nu} b_R) F_{\mu\nu}, & Q_8 &= \frac{g_s}{16\pi^2} m_b (\bar{s}_L \sigma^{\mu\nu} T^a b_R) G_{\mu\nu}^a, \\ Q_9 &= \frac{e^2}{16\pi^2} (\bar{s}_L \gamma_\mu b_L) (\bar{\ell} \gamma^\mu \ell), & Q_{10} &= \frac{e^2}{16\pi^2} (\bar{s}_L \gamma_\mu b_L) (\bar{\ell} \gamma^\mu \gamma_5 \ell), \\ Q_L &= \frac{e^2}{16\pi^2} (\bar{s}_L \gamma_\mu b_L) (\bar{\nu} \gamma^\mu (1 - \gamma_5) \nu). \end{aligned} \quad (3)$$

The dipole operators  $Q_7$  and  $Q_8$  correspond to FCNC  $b \rightarrow s\gamma$  and  $b \rightarrow sg$  vertices, respectively. Semileptonic decays to charged leptons,  $b \rightarrow s\ell^+\ell^-$  involve the operators  $Q_9$  and  $Q_{10}$ ; the corresponding FCNC transitions to neutrinos,  $b \rightarrow s\bar{\nu}\nu$ , are described by  $Q_L$ . Further operators exist that are, however, suppressed in MFV by light quark Yukawas, see Sec. III A, such as the ones obtained from the above (3) by flipping the chiralities of the quark fields. We do not consider NP contributions to those flipped operators, as well as to four-quark operators. Contributions from the latter, however, are taken into account in the SM predictions.

In the fit we also consider the  $B_s - \bar{B}_s$  mass-difference  $\Delta m_s$ , described by the Lagrangian

$$\mathcal{L}_{\text{WET}}^{\text{mix}} = \frac{G_F^2 m_W^2}{16\pi^2} |V_{tb} V_{ts}^*|^2 \sum_i Q_i^{\text{mix}}(\mu) C_i^{\text{mix}}(\mu), \quad (4)$$

where  $m_W$  denotes the mass of the  $W$ -boson, with the operator

$$Q_{V,LL}^{\text{mix}} = (\bar{s}_L \gamma_\mu b_L) (\bar{s}_L \gamma^\mu b_L), \quad (5)$$

and the corresponding Wilson coefficient  $C_{V,LL}^{\text{mix}}$ . Further operators including right-handed quarks are not relevant for our EFT analysis, since right-handed FCNCs are induced at a higher order in the MFV expansion.

We match the SMEFT onto the WET at the one-loop level at the scale  $\mu = m_W$ . The analytic matching conditions are taken from Ref. [31]. They are stated in the appendix VII A for completeness. The numerical matching conditions are presented in the appendix VII B.

### III. MINIMAL FLAVOR VIOLATION IN SMEFT

In this section, we give the flavor ansatz we employ to connect the different sectors, and discuss the phenomenological implications that arise in SMEFT. We start with the MFV ansatz in Sec. III A

and the implementation in SMEFT. In Sec. III B we discuss the rotation to the mass-basis and the resulting phenomenology. We give the parameterization of the flavor structure of Wilson coefficients in Sec. III C.

### A. The MFV ansatz

MFV has been widely used in flavor studies to reduce the number of free parameters and establish connections between various observables. MFV imposes the flavor structure of the SM onto NP, ensuring that FCNCs are controlled by SM parameters, CKM elements and quark masses. Therefore, the scale of NP can be as low as a few TeV, despite the tight constraints from FCNC measurements that would otherwise require NP to be much further away. Formally, MFV requires the SMEFT Lagrangian to respect a  $U(3)^5$  symmetry

$$\mathcal{G}_F = U(3)_{q_L} \times U(3)_{u_R} \times U(3)_{d_R} \times U(3)_{l_L} \times U(3)_{e_R}. \quad (6)$$

In the SM, this symmetry is broken by the SM Yukawa matrices. In MFV, the latter are promoted to spurions, *i.e.*, fictitious fields transforming non-trivially under  $\mathcal{G}_F$ , such that the flavor symmetry is formally restored. The SM fermion fields are charged under  $\mathcal{G}_F$  as

$$\begin{aligned} q_L : (3, 1, 1, 1, 1), & \quad u_R : (1, 3, 1, 1, 1), & \quad d_R : (1, 1, 3, 1, 1), \\ l_L : (1, 1, 1, 3, 1), & \quad e_R : (1, 1, 1, 1, 3), \end{aligned} \quad (7)$$

while the Higgs is a singlet, and the Yukawa spurion fields transform under  $\mathcal{G}_F$  as

$$Y_u : (3, \bar{3}, 1, 1, 1), \quad Y_d : (3, 1, \bar{3}, 1, 1), \quad Y_e : (1, 1, 1, 3, \bar{3}). \quad (8)$$

With this prescription, all terms in the SM Lagrangian are formally invariant under  $\mathcal{G}_F$ . Specifically, the Yukawa terms  $\mathcal{L}_Y = -\bar{q}_L Y_d d_R \varphi - \bar{q}_L Y_u u_R \tilde{\varphi} - \bar{l}_L Y_e e_R \varphi$  respect  $\mathcal{G}_F$  due to the non-trivial transformation of the spurions which cancel the transformations of the fermions.

MFV requires the terms in the SMEFT Lagrangian to be singlets under  $\mathcal{G}_F$ . This implies constraints on the flavor structure of the Wilson coefficients, because they have to cancel the flavor transformations of the fermions in the operators. Denoting Wilson coefficients for the moment generically by  $C_{ij}$ , with flavor indices  $i, j = 1, 2, 3$ , one obtains for the different quark bilinears

$$\bar{q}_L q_L : \quad C_{ij} = \left( a_1 1 + a_2 Y_u Y_u^\dagger + a_3 Y_d Y_d^\dagger + \dots \right)_{ij}, \quad (9a)$$

$$\bar{u}_R u_R : \quad C_{ij} = \left( b_1 1 + b_2 Y_u^\dagger Y_u + \dots \right)_{ij}, \quad (9b)$$

$$\bar{q}_L u_R: \quad C_{ij} = \left( \left( c_1 1 + c_2 Y_u Y_u^\dagger + \dots \right) Y_u \right)_{ij}, \quad (9c)$$

$$\bar{q}_L d_R: \quad C_{ij} = \left( \left( d_1 1 + d_2 Y_u Y_u^\dagger + \dots \right) Y_d \right)_{ij}, \quad (9d)$$

$$\bar{d}_R d_R: \quad C_{ij} = \left( e_1 1 + e_2 Y_d^\dagger Y_d + \dots \right)_{ij}, \quad (9e)$$

where the ellipsis indicate higher order terms. The MFV coefficients  $a_k, b_k, c_k, d_k, e_k$  parameterize the flavor structure of the quark bilinears. It is sensible to use identical MFV coefficients for all operators containing a given bilinear up to an overall, operator-dependent Wilson coefficient <sup>1</sup>. Such a universal flavor structure originates from flavor symmetry, under which all operators of type  $\bar{q}qX$  with any flavor singlet  $X$  have the same transformation properties. This allows for a significant reduction in the number of fit parameters. On the other hand, universality is not exact. It receives radiative corrections from electroweak loops and Yukawa-induced mixing with other operators [27, 28], noting also that Froggatt-Nielsen flavor symmetries generically only provide patterns accurate up to numbers of order one, effects of which are not considered in our analysis. Models with multi-messengers <sup>2</sup>, which transform non-trivially under  $\mathcal{G}_F$  can be constructed that also break universality. An example is a  $Z'$  that couples flavor-blind to  $\bar{q}_L q_L$  and both  $\bar{e}_R e_R$  and  $\bar{l}_L l_L$ , together with a leptoquark that couples to  $\bar{q}_L l_L$  transforming as  $u_R \bar{l}_L$ , that is, as  $(1, 3, 1, \bar{3}, 1)$ , hence with a Yukawa coupling proportional to  $Y_u$ . The leptoquark induces  $a_2$  in  $C_{lq}$  only, whereas the  $Z'$  feeds into  $a_1$  of both  $C_{lq}$  and  $C_{qe}$ . We do find, however, from the actual analysis that our simplified ansatz employed for  $\bar{q}_L q_L$  and  $\bar{u}_R u_R$  and confronted to present experimental sensitivities leads to a convergent fit <sup>3</sup>. We hope to come back to fits with more parameters (from flavor, or further operators) and improved data in the future.

The lepton flavor structure can be analogously expressed in terms of  $Y_e$  as

$$\bar{l}_L l_L: \quad C_{ij} = \left( f_1 1 + f_2 Y_e Y_e^\dagger + \dots \right)_{ij}, \quad (10a)$$

$$\bar{e}_R e_R: \quad C_{ij} = \left( g_1 1 + b_2 Y_e^\dagger Y_e + \dots \right)_{ij}, \quad (10b)$$

$$\bar{l}_L e_R: \quad C_{ij} = \left( \left( h_1 1 + h_2 Y_e Y_e^\dagger + \dots \right) Y_e \right)_{ij}. \quad (10c)$$

It has been pointed out that the a priori infinite series in Eq. (9) can be resummed by using the Cayley-Hamilton identity [30, 32]. This results in a finite number of terms, indicating that in principle any BSM model can be parameterized according to the MFV expansion in Eqs. (9) if

<sup>1</sup> Four-quark operators in MFV are analyzed in [12].

<sup>2</sup> We are grateful to the unknown referee for this comment.

<sup>3</sup> In our subsequent analysis we neglect the lepton Yukawas hence (9) also includes semileptonic four-fermion operators.

MFV coefficients  $a_k, b_k, c_k, d_k, e_k$  of arbitrary size are allowed. Hence, MFV can be viewed as a parameterization of the BSM flavor structure rather than a restriction. The relative magnitude of the expansion parameters becomes then of interest, as it provides insights into the flavor structure of BSM physics. Specifically, textures  $|a_{k \geq 2}| \lesssim |a_1|$ , that is, with a dominant first order term, and similarly for the other currents, correspond to a more SM-like pattern, that features near-universality and suppressed FCNCs.

## B. Mass basis

To apply the MFV ansatz to the fit, the flavor-basis expansion in Eq. (9) has to be given in the mass basis of the fermions. We write the transformation from flavor to mass eigenstates (primed fields) for the quarks as

$$u_L = S_L^u u'_L, \quad d_L = S_L^d d'_L, \quad u_R = S_R^u u'_R, \quad d_R = S_R^d d'_R, \quad (11)$$

where the unitary matrices  $S_{L,R}^{u,d}$  are obtained from the diagonalization of Yukawa matrices,

$$Y_u^{\text{diag}} = S_L^{u\dagger} Y_u S_R^u, \quad Y_d^{\text{diag}} = S_L^{d\dagger} Y_d S_R^d, \quad (12)$$

with the diagonal (mass basis) matrices given by the quark masses

$$Y_u^{\text{diag}} = \sqrt{2}/v \text{diag}(m_u, m_c, m_t) \quad Y_d^{\text{diag}} = \sqrt{2}/v \text{diag}(m_d, m_s, m_b). \quad (13)$$

As we neglect lepton masses there is no corresponding transformation in this sector.

In contrast to the top-philic approach, the choice of a mass basis – up mass or down mass basis – does not affect the phenomenology in the MFV scenario. This is similar to the SM, where only the CKM-matrix defined as

$$V = (S_L^u)^\dagger S_L^d, \quad (14)$$

is physical, while the individual rotation matrices  $S_L^{u/d}$  and  $S_R^{u/d}$  cannot be probed. To demonstrate this point, let us consider an operator containing two left-handed quark doublets in the flavor basis

$$C_{ij} \bar{q}_{L_i} q_{L_j} = \bar{q}_{L_i} \left[ a_1 1 + a_2 Y_u Y_u^\dagger + a_3 Y_d Y_d^\dagger \right]_{ij} q_{L_j}. \quad (15)$$

After the rotation to the mass basis, we obtain for the up-type quarks

$$C_{ij} \bar{q}_{L_i} q_{L_j} \supset \bar{u}'_{L_i} S_{L_{ik}}^{u\dagger} \left[ a_1 1 + a_2 S_L^u (Y_u^{\text{diag}}) S_R^{u\dagger} S_R^u (Y_u^{\text{diag}}) S_L^{u\dagger} \right. \\ \left. + a_3 S_L^d (Y_d^{\text{diag}}) S_R^{d\dagger} S_R^d (Y_d^{\text{diag}}) S_L^{d\dagger} \right]_{km} S_{L_{mj}}^u u'_{L_j}, \quad (16)$$



and for the down-type quarks

$$C_{ij} \bar{q}_{L_i} q_{L_j} \supset \bar{d}'_{L_i} S_{L_{ik}}^{d\dagger} \left[ a_1 1 + a_2 S_L^u (Y_u^{\text{diag}}) S_R^{u\dagger} S_R^u (Y_u^{\text{diag}}) S_L^{u\dagger} \right. \\ \left. + a_3 S_L^d (Y_d^{\text{diag}}) S_R^{d\dagger} S_R^d (Y_d^{\text{diag}}) S_L^{d\dagger} \right]_{km} S_{L_{mj}}^d d'_{L_j}. \quad (17)$$

Using unitarity and Eq. (14), these expressions can be simplified to

$$C_{ij} \bar{q}_{L_i} q_{L_j} \supset \bar{u}'_{L_i} \left[ a_1 1 + a_2 [Y_u^{\text{diag}}]^2 + a_3 V [Y_d^{\text{diag}}]^2 V^\dagger \right]_{ij} u'_{L_j} \\ + \bar{d}'_{L_i} \left[ a_1 1 + a_2 V^\dagger [Y_u^{\text{diag}}]^2 V + a_3 [Y_d^{\text{diag}}]^2 \right]_{ij} d'_{L_j}, \quad (18)$$

which are independent of whether flavor originates from the up or the down sector.

In this work, we neglect all Yukawa couplings except for the one of the top  $y_t = \sqrt{2}m_t/v$ , *i.e.*, we use

$$Y_e = 0, \quad Y_d = 0, \quad Y_u = \text{diag}(0, 0, y_t). \quad (19)$$

With these assumptions, a rotation of the quark bilinears in (9) to the mass basis yields

$$\bar{d}'_{L_i} d_{L_j} : a_1 \delta_{ij} + a_2 y_t^2 V_{ti}^* V_{tj}, \quad \bar{u}_{L_i} u_{L_j} : a_1 \delta_{ij} + a_2 y_t^2 \delta_{3i} \delta_{3j}, \quad (20)$$

$$\bar{u}_{R_i} u_{R_j} : b_1 \delta_{ij} + b_2 y_t^2 \delta_{3i} \delta_{3j}, \quad \bar{d}'_{R_i} d_{R_j} : e_1 \delta_{ij}, \quad (21)$$

$$\bar{u}_{L_i} d_{L_j} : a_1 V_{ij} + a_2 y_t^2 \delta_{3i} V_{tj}, \quad \bar{d}'_{L_i} u_{L_j} : a_1 V_{ji}^* + a_2 y_t^2 V_{ti}^* \delta_{3j}, \quad (22)$$

$$\bar{u}_{L_i} u_{R_j} : (c_1 + c_2 y_t^2) y_t \delta_{3i} \delta_{3j}, \quad \bar{d}'_{L_i} u_{R_j} : (c_1 + c_2 y_t^2) y_t V_{ti}^* \delta_{3j}, \quad (23)$$

$$\bar{d}'_{L_i} d_{R_j} : \simeq 0, \quad \bar{u}_{L_i} d_{R_j} : \simeq 0. \quad (24)$$

Neglecting the down-Yukawa switches off chirality-flipping interactions in the down-quark sector. While left-handed down-type FCNCs  $d_{L_j} \rightarrow d_{L_i}$  proportional to  $a_2 y_t^2 V_{ti}^* V_{tj}$  are induced in this setup, no up-type or right-handed down-type FCNCs arise. Neglecting the masses of the leptons switches off chirality-flipping interactions among leptons, and the chirality-conserving lepton bilinears are flavor diagonal and universal

$$\bar{l}_{L_i} l_{L_j} : f_1 \delta_{ij}, \quad \bar{e}_{R_i} e_{R_j} : g_1 \delta_{ij}, \quad \bar{l}_{L_i} e_{R_j} : \simeq 0. \quad (25)$$

Let us comment on (19), that is, neglecting the lepton and down-type quark Yukawas in SMEFT. While these couplings are subdominant in single-Higgs models (13), they can be parametrically enhanced in multi-Higgs models, for example, the Minimal Supersymmetric Standard Model by ratios of vacuum expectation values. In any case, for  $Y_d \neq 0$  and  $Y_e \neq 0$  chirality flipping operators arise which contribute at tree-level to the anomalous moments of the leptons, and radiative  $B$ -decays. Since presently no new physics in these observables has been established, we focus on

the set-up (1), targeting semileptonic  $B$ -decays and top-observables, among others. In principle further SMEFT operators can and ideally should be taken into account in future works to make the analysis more model-independent. However, this comes at the price of a significant step in complexity regarding the number of degrees of freedom, their correlation and the measurements, which is beyond the scope of this analysis.

### C. Parameterization in the fit

As customary in SMEFT studies, we rescale the Wilson coefficients by  $v^2/\Lambda^2$ , generically,

$$\tilde{C} = \frac{v^2}{\Lambda^2} C. \quad (26)$$

Concerning the MFV flavor structure, inspecting the  $\bar{q}_L q_L$  bilinears in Eq. (20), relevant for the operators  $O_{\varphi q}^{(1)}$ ,  $O_{\varphi q}^{(3)}$ ,  $O_{qe}$ ,  $O_{lq}^{(1)}$ , and  $O_{lq}^{(3)}$ , we see that those involving top quarks are multiplied by  $a_1 + a_2 y_t^2$ . In contrast, the flavor-conserving operators containing up-type quarks of the first or second generation receive a contribution from the leading term of the MFV expansion only,  $a_1$ . We absorb the latter into the rescaled Wilson coefficient for left-handed up-type first and second generation bilinears as

$$\tilde{C}_{q\bar{q}} = \frac{v^2}{\Lambda^2} a_1. \quad (27)$$

The Wilson coefficient for processes involving left-handed top quarks is then given by

$$\tilde{C}_{q\bar{q}} \left( 1 + \frac{a_2 y_t^2}{a_1} + \frac{a_4 y_t^4}{a_1} + \dots \right) = \tilde{C}_{q\bar{q}} (1 + \gamma_a) \quad (28)$$

with

$$\gamma_a = \sum_{n \geq 1} y_t^{2n} a_{2n} / a_1. \quad (29)$$

Note that all higher orders of the top-Yukawa with terms  $a_{2n} (Y_u Y_u^\dagger)^n$  in the spurion expansion can be absorbed into  $\gamma_a$  as they lead to the same flavor structure as the leading correction  $a_2 Y_u Y_u^\dagger$ . The ratio  $\gamma_a$  is universal for all operators containing a  $\bar{q}_L q_L$  structure. In our setup, this parameter represents the relative strength of the NP coupling to left-handed third-generation quark-doublets compared to the flavor-diagonal coupling. As such, it provides an indirect probe of the flavor structure of BSM physics.

We can test  $\gamma_a$  in a combined fit to  $b \rightarrow s$  FCNC processes, Drell-Yan production, and  $t\bar{t}$  observables with sensitivity to the same Wilson coefficients, but different combinations of  $\tilde{C}_{q\bar{q}}$  and

$\gamma_a$ . For instance, the left-handed down-type FCNC coupling  $\bar{d}_i d_j, i \neq j$  is directly proportional to  $\gamma_a$  and parameterized by  $\tilde{C}_{q\bar{q}} \gamma_a V_{ti}^* V_{tj}$ . On the other hand, Drell-Yan production with flavor-diagonal up-type quarks in the initial state multiplies probes  $\tilde{C}_{q\bar{q}}$ , while left-handed down-type diagonal couplings  $\bar{d}_i d_i$  are proportional to  $\tilde{C}_{q\bar{q}}(1 + \gamma_a |V_{ti}|^2)$ .

For right-handed tops we employ a parameterization analogous to (28) using (21) for the  $\bar{u}_{R3} u_{R3}$  currents

$$\tilde{C}_{u\bar{u}} \left( 1 + \frac{b_2 y_t^2}{b_1} + \frac{b_4 y_t^4}{b_1} + \dots \right) = \tilde{C}_{u\bar{u}} (1 + \gamma_b) \quad (30)$$

with

$$\gamma_b = \sum_{n \geq 1} y_t^{2n} b_{2n} / b_1, \quad (31)$$

and the coefficient for the first and second generation currents  $\bar{u}_{Ri} u_{Ri}, i = 1, 2$ ,

$$\tilde{C}_{u\bar{u}} = \frac{v^2}{\Lambda^2} b_1. \quad (32)$$

Again, all higher powers of the top-Yukawa with terms  $b_{2n} (Y_u^\dagger Y_u)^n$  can be absorbed into  $\gamma_b$  as they lead to the same flavor structure as the leading correction  $b_2 Y_u^\dagger Y_u$ . A similar argument holds for the dipole operators of the type  $\bar{q}_L u_R$ , which comprise the operators  $O_{uB}, O_{uG}$  and  $O_{uW}$ . In MFV, these couplings are proportional to  $Y_u$ . Hence, these operators only induce a coupling to top quarks that is proportional to the rescaled coefficient  $\tilde{C}_{q\bar{u}} = \frac{v^2}{\Lambda^2} y_t (c_1 + c_2 y_t^2 + c_4 y_t^4 \dots)$ .

The right-handed down-quark bilinear  $\bar{d}_R d_R$  is relevant for the operators  $O_{\varphi d}, O_{ed}$  and  $O_{ld}$ . Since we neglect the down-type Yukawas, only the rescaled universal and flavor-diagonal coefficient at leading order MFV  $\tilde{C}_{d\bar{d}} = \frac{v^2}{\Lambda^2} e_1$  contributes as an additional degree of freedom in the fit.

The lepton flavor bilinears that enter the semileptonic four-fermion operators comprise only lepton flavor-diagonal couplings due to the vanishing lepton Yukawas in our setup (19). Hence, the respective MFV coefficients  $f_i$  and  $g_i$  can simply be absorbed into the Wilson coefficients, resulting in a lepton-flavor universal scenario.

To summarize, we end up with in total 16 degrees of freedom in the full fit – 14 Wilson coefficients  $\tilde{C}_i$  and two flavor ratios  $\gamma_{a,b}$ .

#### IV. SIMULATION AND MEASUREMENTS

In this section, we describe the computation of the theory predictions for the different observables and discuss their sensitivity to the SMEFT Wilson coefficients. In general, a cross section in the

SMEFT framework can be parameterized in terms of the Wilson coefficients as

$$\sigma = \sigma^{\text{SM}} + \frac{1}{\Lambda^2} \sum_i \tilde{C}_i \sigma_i^{\text{int}} + \frac{1}{\Lambda^4} \sum_{i \leq j} \tilde{C}_i \tilde{C}_j \sigma_{ij}^{\text{BSM}}. \quad (33)$$

with the SM cross section  $\sigma^{\text{SM}}$ , the interference terms  $\sigma_i^{\text{int}}$  between the SMEFT and the SM, and the pure SMEFT contribution  $\sigma_{ij}^{\text{BSM}}$ . The latter includes the contribution of the individual operators squared as well as the interference between different SMEFT operators. The interference terms between dimension-eight operators and the SM, which are formally of the same order  $1/\Lambda^4$  in the expansion as the dimension-six terms squared, are neglected in this work. Quantifying the impact of dimension-eight operators on fits in general requires a case by case study as it depends on the processes and operators considered as well as the scale separation [33–37]: The larger the separation between  $\Lambda$  and the energy of the process, the smaller the impact. The impact also drops if dimension-six and dimension-eight operators are correlated [22]. As the number of operators at higher dimension quickly rises, to make progress we restrict ourselves in our analysis to the leading operators in the SMEFT.

Alternatively, one could stop in (33) at order  $1/\Lambda^2$  at the level of the cross section, that is, discard the pure BSM contribution  $\sigma_{ij}^{\text{BSM}}$ . Analyses of single-top production data from the LHC reveal that the constraints on dimension-six operators with or without quadratic  $1/\Lambda^4$  terms are in very good agreement, indicating that the impact of partial higher order EFT corrections is subleading here [38]. On the other hand, the quadratic terms are important for Drell-Yan production, since for the FCNC quark flavor combinations the interference terms with the SM are negligible.

For the computation of the partonic cross sections of collider observables, we employ MADGRAPH5\_aMC@NLO [39, 40] with the NN23LO PDF set [41] as implemented in LHAPDF 6 [42]. The SMEFT contributions  $\sigma_i^{\text{int}}$  and  $\sigma_{ij}^{\text{BSM}}$  for the top, Drell-Yan and  $Z$ -decay observables employed in the global fit are generated with the predefined UFO model `SMEFTsim 3.0` [25, 43], whereas the top-quark observables "Before 2021" in Sec. V A are computed with the `dim6top_L0` UFO model [14]. As a first step, we validate our setup by reproducing the SM predictions. We find an agreement within 20% for all collider observables, which is reasonable since we do not consider higher-order corrections and have only limited statistics for the Monte Carlo data. In the high- $p_T$  and invariant-mass tails of the distributions, which are most relevant due to the energy enhancement, the precision is comparable to the experimental uncertainty. In the fits we include the recent SM predictions [44–53]. We further consider only the most precise measurement of each individual process, as correlations among different experiments can have a significant impact on the fit [38].

### A. Top quark observables

We consider inclusive cross sections of  $t\bar{t}H$  and  $t\bar{t}W$  production as well as the differential  $t\bar{t}$ ,  $t\bar{t}Z$  and  $t\bar{t}\gamma$  cross section measurements. In addition, we also include the decay width of the top quark,  $\Gamma_t$ , and the  $W$ -boson helicity fractions  $f_0$  and  $f_L$ . The decay width and the helicity fractions are computed following Ref. [54] including quadratic SMEFT contributions. For the computation of the inclusive  $t\bar{t}H$  and  $t\bar{t}W$  cross sections, we generate 50 000 events at leading order (LO) for each operator. In order to compute the differential cross sections of the  $t\bar{t}$ ,  $t\bar{t}Z$  and  $t\bar{t}\gamma$  processes, we generate an inclusive sample with 200 000 events for each observable. These samples are subsequently binned with regard to the differential observable of interest, which is the mass of the  $t\bar{t}$  pair, the  $p_T$  of the  $Z$  boson, and the  $p_T$  of the photon, respectively. The binning is performed with MadAnalysis 5 [55] according to the binning employed in the experimental analyses.

In general, a linear combination of several Wilson coefficients contributes to a given observable. In the case of associated top-quark pair production, these linear combinations are given by

$$\begin{aligned}\tilde{C}_{uZ} &= -\sin\theta_w\tilde{C}_{uB} + \cos\theta_w\tilde{C}_{uW}, & \tilde{C}_{\varphi q}^- &= \tilde{C}_{\varphi q}^{(1)} - \tilde{C}_{\varphi q}^{(3)}, \\ \tilde{C}_{u\gamma} &= \cos\theta_w\tilde{C}_{uB} + \sin\theta_w\tilde{C}_{uW},\end{aligned}\tag{34}$$

with the weak mixing angle  $\theta_w$ . The observables, sensitivities and corresponding measurements of the top-quark sector are summarized in Tab. I.

Process	Observable	SMEFT operators	Experiment	Ref.	SM Ref.
$t\bar{t}$	$\frac{d\sigma}{dm(t\bar{t})}$	$\tilde{C}_{uG}$	CMS	[44]	[44]
$t\bar{t}Z$	$\frac{d\sigma}{dp_T(Z)}$	$\tilde{C}_{uG} \tilde{C}_{uZ} \tilde{C}_{\varphi u} \tilde{C}_{\varphi q}^-$	ATLAS	[56]	[45]
$t\bar{t}\gamma$	$\frac{d\sigma}{dp_T(\gamma)}$	$\tilde{C}_{uG} \tilde{C}_{u\gamma}$	ATLAS	[57]	[46]
$t\bar{t}W$	$\sigma_{t\bar{t}W}$	$\tilde{C}_{uG}$	ATLAS	[58]	[47]
$t\bar{t}H$	$\sigma_{t\bar{t}H} \times B_{\gamma\gamma}$	$\tilde{C}_{uG}$	ATLAS	[48]	[48]
$t \rightarrow Wb$	$f_0, f_L$	$\tilde{C}_{uW}$	ATLAS	[59]	[49]
$t \rightarrow Wb$	$\Gamma_t$	$\tilde{C}_{uW} \tilde{C}_{\varphi q}^3$	ATLAS	[59]	[49]

TABLE I: Observables, sensitivities and references for the measurements as well as the SM predictions of  $t\bar{t}$  processes and top-quark decays included in this analysis. All measurements are carried out at  $\sqrt{s} = 13$  TeV.

## B. Drell-Yan observables

We implement differential distributions of the neutral-current (NC)  $pp \rightarrow \ell^+ \ell^-$  and the charged-current (CC)  $pp \rightarrow \ell \nu$  Drell-Yan processes for each lepton flavor  $\ell = e, \mu, \tau$ . The measurements included in the fit are listed in Tab. II together with the corresponding integrated luminosity.

Process	Experiment	Ref.	int. Lum.	Process	Experiment	Ref.	int. Lum.
$pp \rightarrow e^+ e^-$	CMS	[50]	137 fb <sup>-1</sup>	$pp \rightarrow e \nu$	ATLAS	[52]	139 fb <sup>-1</sup>
$pp \rightarrow \mu^+ \mu^-$	CMS	[50]	140 fb <sup>-1</sup>	$pp \rightarrow \mu \nu$	ATLAS	[52]	139 fb <sup>-1</sup>
$pp \rightarrow \tau^+ \tau^-$	ATLAS	[51]	139 fb <sup>-1</sup>	$pp \rightarrow \tau \nu$	ATLAS	[53]	139 fb <sup>-1</sup>

TABLE II: References to the measurements of the NC (left) and CC (right) DY process together with the corresponding integrated luminosity. All measurements are carried out at  $\sqrt{s} = 13$  TeV.

The Drell-Yan process at LO is sensitive to all Wilson coefficients in (1) except for the dipole operators. These do not contribute to the LO Drell-Yan process in our parameterization, because the only non-vanishing Yukawa coupling in our setup is the top-Yukawa (19). The strongest Drell-Yan constraints arise for semileptonic four-fermion operators, since they grow with energy as  $\mathcal{O}(s/\Lambda^2)$  [36] and thus generate large contributions in the high- $p_T$  tails where the SM contribution is small. The vertex-correcting penguin operators, on the other hand, only alter the coupling of the  $W$  and  $Z$  boson to quarks with respect to the SM coupling. As the energy exceeds the electroweak scale, the contributions from both these operators decrease.

Due to the high momenta of particles at the LHC, different chirality states can be regarded as independent particles. Therefore, the interference terms between operators comprising different chiralities of quarks and leptons vanish and only interference terms between the left-handed singlet and triplet operators  $O_{lq}^{(1)}$  and  $O_{lq}^{(3)}$  as well as  $O_{\varphi q}^{(1)}$  and  $O_{\varphi q}^{(3)}$  are present. Hence, several Wilson coefficients can be constrained individually without having issues with large cancellations, *i.e.*, flat directions in the parameter space.

With the Drell-Yan process, five different initial state quarks can be accessed in the proton, whose composition is described by the parton distribution functions (PDFs). We define the parton-parton luminosity  $\mathcal{L}_{q_i \bar{q}_j}$  for a collision of a quark  $q_i$  with an antiquark  $\bar{q}_j$ ,

$$\mathcal{L}_{q_i \bar{q}_j} = \tau \int_{\tau}^1 \frac{dx}{x} [f_{q_i}(x, \mu_F) f_{\bar{q}_j}(\tau/x, \mu_F) + f_{\bar{q}_j}(x, \mu_F) f_{q_i}(\tau/x, \mu_F)] , \quad (35)$$

where  $\tau = \hat{s}/s$  [21]. Here,  $f_{q_i}$  denotes the PDF of the quark  $q_i$ ,  $\mu_F$  is the factorization scale and  $\sqrt{s}$  and  $\sqrt{\hat{s}}$  refer to the proton-proton and partonic center-of-mass energy, respectively. The

parton-parton luminosities in Eq. (35) allow to obtain the Drell-Yan cross sections  $\sigma(pp \rightarrow \ell\ell)$  and  $\sigma(pp \rightarrow \ell\nu)$  from the partonic cross section  $\hat{\sigma}$  as

$$\sigma = \sum_{ij} \int \frac{d\tau}{\tau} \mathcal{L}_{q_i\bar{q}_j}(\tau) \hat{\sigma}(\tau s). \quad (36)$$

The sum includes all quark combinations appropriate for CC or NC currents except for the top.

The parton-parton luminosities for the different NC quark combinations are shown in Fig. 1, and for the CC combinations in Fig. 2 as a function of the partonic center-of-mass energy  $\sqrt{\hat{s}}$ . We use the PDF set NN23LO [41] and show  $1\sigma$  ranges (shaded bands) and central values (dark solid or dashed lines). To illustrate the impact of the various flavor combinations on the global MFV fit, the CC parton-parton luminosities are weighted by a factor  $|V_{ij}|$  for  $u_i\bar{d}_j$  or  $\bar{u}_i d_j$  fusion. This CKM factor arises from the MFV parameterization in Eq. (22), resulting in a suppression of CC transitions, similar to the SM. For the FCNC combinations, the interference term between the SM and the SMEFT amplitude is absent, so that no contribution linear in  $\tilde{C}$  arises. Thus, we weight the corresponding FCNC parton-parton luminosities by  $|V_{ti}V_{tj}|^2$ , the modulus-squared of the term proportional to  $a_2$ , see (20). For the CC and FCNC combinations that include an up or a down quark, the parton-parton luminosities of the charge-conjugated combination are visualized with dashed lines. If no up or down quark is present, the luminosities of the charge-conjugated processes are identical, since the PDFs of sea-quarks are equal to those of their antiquarks. For the up and down quark, however, which constitute the valence quarks of the proton, the PDF of the quark is significantly larger than the PDF of the related anti-quark, resulting in a difference between the charge conjugated parton-parton-luminosities. Our  $\mathcal{L}_{q_i\bar{q}_j}$  are consistent with Ref. [21].

In contrast to the top-quark observables, the Drell-Yan measurements included in our analysis are not unfolded, so that hadronization and detector effects have to be taken into account. As the number of events is directly proportional to the cross section, a parameterization of the total event number analogous to Eq. (33) can be employed. We simulate the SMEFT contribution to the cross section separated into the different initial-state quark flavor compositions. We generate 400 000 events for every operator and every initial-state flavor combination in order to ensure a sufficiently high number of events in the high- $p_T$  tails. Here, the statistics of the samples are typically diminished, resulting from the PDF-suppression at high momentum fractions. We employ PYTHIA 8.3 [60] to simulate the parton shower and hadronization. Detector effects are included by performing a parametric detector simulation with DELPHES3 [61]. The signal extraction is carried out with ROOT [62], following the analysis strategy and the cuts outlined in the corresponding experimental analysis.

We assume that the background events are predominantly accounted for by the SM, so that any potential NP contributions to the background are neglected. This simplification seems acceptable considering that in most analyses, the Drell-Yan production cross section is assumed to dominate over the sum of all background contributions. Only in the  $\tau\tau$ -channel, a significant fraction of the events are attributed to jets faking hadronic  $\tau$ -leptons, which might potentially be altered by NP contributions in multijet production. These effects have, however, already been investigated and are tightly constrained [63].

The NC Drell-Yan process is sensitive to all semileptonic four-fermion operators as well as to the two-fermion penguin-operators. For operators comprising two left-handed quark doublets, the

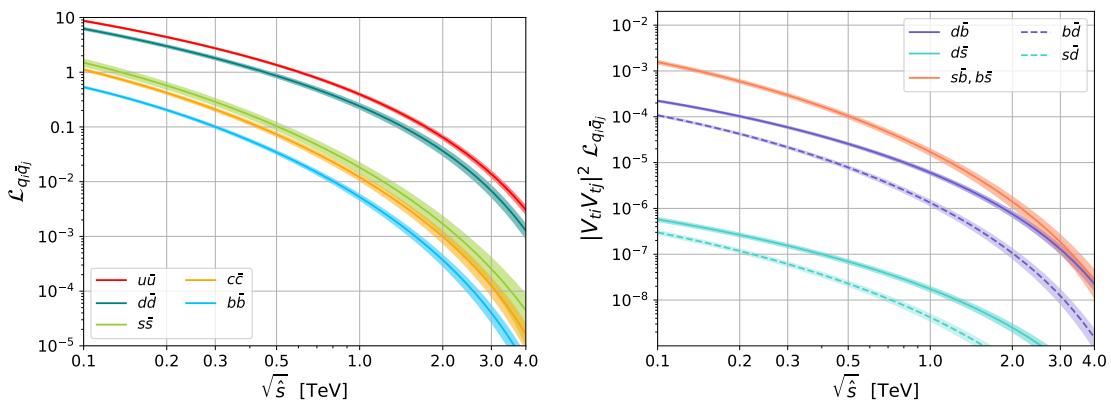


FIG. 1: Parton-parton luminosities of the quark combinations contributing to the flavor-diagonal NC (left panel) and FCNC (right panel) Drell-Yan process. The FCNC combinations are scaled by  $|V_{ti}V_{tj}|^2$  to illustrate the impact on the MFV fit. Shaded bands correspond to  $1\sigma$  ranges and dark solid or dashed lines to central values.

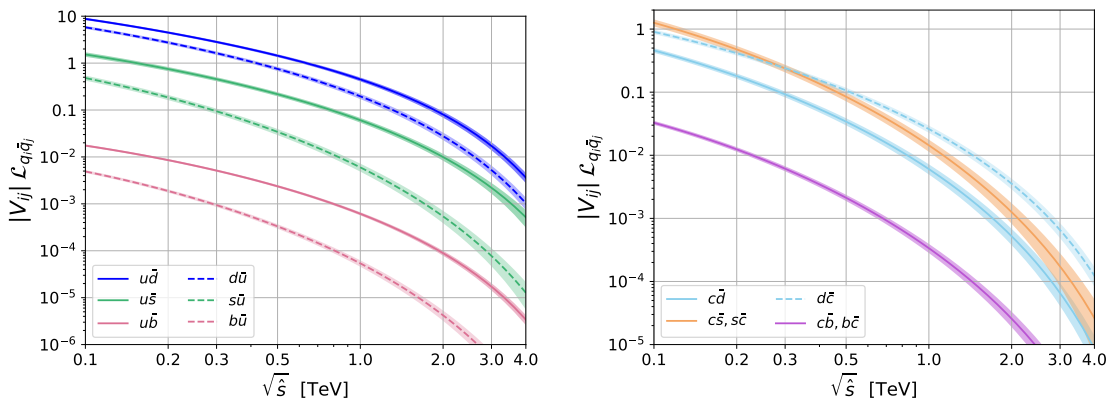


FIG. 2: Parton-parton luminosities of the quark combinations contributing to the CC Drell-Yan process scaled by  $|V_{ij}|$  including  $u$ , or  $\bar{u}$  quarks (left panel) and  $c$ , or  $\bar{c}$  quarks (right panel). Shaded bands correspond to  $1\sigma$  ranges and dark solid or dashed lines to central values.



linear combinations

$$\tilde{C}_{\varphi q}^+ = \tilde{C}_{\varphi q}^{(1)} + \tilde{C}_{\varphi q}^{(3)} \quad \tilde{C}_{\varphi q}^- = \tilde{C}_{\varphi q}^{(1)} - \tilde{C}_{\varphi q}^{(3)} \quad (37)$$

$$\tilde{C}_{lq}^+ = \tilde{C}_{lq}^{(1)} + \tilde{C}_{lq}^{(3)} \quad \tilde{C}_{lq}^- = \tilde{C}_{lq}^{(1)} - \tilde{C}_{lq}^{(3)} \quad (38)$$

contribute to the NC process. The combinations  $\tilde{C}_{\varphi q}^+$  and  $\tilde{C}_{lq}^+$  are sensitive to the DY process with down-type quarks in the initial state, while  $\tilde{C}_{\varphi q}^-$  and  $\tilde{C}_{lq}^-$  can be probed with initial-state up-type quarks. The CC process, in contrast, is only sensitive to the triplet Wilson coefficients  $\tilde{C}_{\varphi q}^{(3)}$  and  $\tilde{C}_{lq}^{(3)}$ . This adds another linearly independent direction in the parameter space of the Drell-Yan fit, which further improves the bounds.

With regard to the large partonic center-of-mass energy that can be accessed with the tails of Drell-Yan measurements, a sufficiently high value for  $\Lambda$  has to be assumed in order to ensure the validity of the EFT approach. We therefore set the NP scale to  $\Lambda = 10$  TeV in all fits <sup>4</sup>.

### C. Z-pole observables

We incorporate the  $Z \rightarrow b\bar{b}$  observables  $A_{\text{FB}}^b$  and  $R_b$ , denoting the forward-backward asymmetry and the ratio of  $Z \rightarrow b\bar{b}$  to  $Z \rightarrow \text{hadrons}$ , respectively, as well as the corresponding  $Z \rightarrow c\bar{c}$  observables  $A_{\text{FB}}^c$  and  $R_c$  into the fit. The  $c\bar{c}$ -couplings probed by the latter are given by the diagonal terms of the left- and right-handed up-type quark couplings in the MFV parameterization Eqs. (20) and (21). These couplings are absent in the top-philic scenario, marking a significant difference between the two flavor patterns.

The Z-pole observables provide important constraints on the penguin operators, in particular for  $O_{\varphi u}$  and  $O_{\varphi d}$  with coupling to right-handed quarks, which are otherwise only weakly constrained by Drell-Yan and  $b \rightarrow s$  observables.

For the computation of the asymmetry observables and the ratios we employ `flavio` [64], whereas the SMEFT contributions to the hadronic cross section are simulated using `MADGRAPH5_aMC@NLO` with the `SMEFTsim 3.0` UFO model [25, 43]. For the fit we take into account the combined LEP-measurement, including correlations [65]

$$\begin{aligned} A_{\text{FB}}^b &= 0.0992 \pm 0.0016, & R_b &= 0.21629 \pm 0.00066, \\ A_{\text{FB}}^c &= 0.0707 \pm 0.0035, & R_c &= 0.1721 \pm 0.0030. \end{aligned} \quad (39)$$

<sup>4</sup> In Figs. 3-11 we provide constraints on the rescaled Wilson coefficients  $\tilde{C}$ , see Eq. (26) at the scale  $\mu = \Lambda = 10$  TeV. At the technical level we sample the coefficients at that scale and RG-evolve them to the weak scale to make contact with data. A larger value of  $\Lambda$  hence simply means more RG-running and operator mixing.

### D. $B$ -physics observables

We follow Ref. [13] and consider various  $B$ -physics observables involving  $b \rightarrow s\gamma$  and  $b \rightarrow s\ell^+\ell^-$  transitions along with  $B_s$ -meson mixing. These include (differential) branching ratios and angular observables, as well as the  $B_s - \bar{B}_s$ -mass difference  $\Delta m_s$ . The WET contributions to these observables are computed using `flavio` [64] together with the Python package `wilson` [29] as described in Ref. [13]. Details on the  $B \rightarrow K$  form factors are provided in App.VIID. For the  $B \rightarrow K^*$  form factors, we employ a combined fit [66] to Light-Cone Sum Rules [66] and lattice QCD [67] results. The observables and measurements are compiled in Tab. III.

In contrast to Ref. [13], the measurements of the  $B_s \rightarrow \phi\mu^+\mu^-$  observables as well as the branching ratio  $B_s \rightarrow \mu^+\mu^-$  have been updated. The latter has recently been measured by CMS [68] and the experimental value is now closer to SM prediction [69], compared to the previous result by LHCb [70]. We employ only the more precise CMS result, as no combined world average is available, and correlations matter [38]. An overview of the Wilson coefficients probed in the  $B$ -observables is given in Tab. IV.

Process	Observable	$q^2$ [GeV <sup>2</sup> ]	Collaboration	Ref.	SM Ref.
$\bar{B} \rightarrow X_s\gamma$	$\mathcal{B}_{E_\gamma > 1.6 \text{ GeV}}$		HFLAV	[71]	[72]
$B^0 \rightarrow K^*\gamma$	$\mathcal{B}$		HFLAV	[71]	[64]
$B^+ \rightarrow K^{*+}\gamma$	$\mathcal{B}$		HFLAV	[71]	[64]
$\bar{B} \rightarrow X_s\ell^+\ell^-$	$\mathcal{B}$	[1, 6]	BaBar	[73]	[75]
	$A_{\text{FB}}$		Belle	[74]	
$B_s \rightarrow \mu^+\mu^-$	$\mathcal{B}$		CMS	[68]	[69]
$B^0 \rightarrow K^*\mu^+\mu^-$	$F_L, P_1, P_2, P_3,$	[1.1, 6]	LHCb	[76]	[64]
	$P'_4, P'_5, P'_6, P'_8$				
$B^0 \rightarrow K\mu^+\mu^-$	$d\mathcal{B}/dq^2$	[1, 6]	LHCb	[77]	[64]
$B^+ \rightarrow K^+\mu^+\mu^-$	$d\mathcal{B}/dq^2$	[1, 6]	LHCb	[77]	[64]
$B^+ \rightarrow K^{*+}\mu^+\mu^-$	$d\mathcal{B}/dq^2$	[1, 6]	LHCb	[77]	[64]
$B_s \rightarrow \phi\mu^+\mu^-$	$F_L, S_3, S_4, S_7$	[1.1, 6]	LHCb	[78]	[64]
$\Lambda_b \rightarrow \Lambda\mu^+\mu^-$	$d\mathcal{B}/dq^2$	[15, 20]	LHCb	[79]	[64]
$B_s - \bar{B}_s$ mixing	$\Delta m_s$		HFLAV	[71]	[80]

TABLE III:  $B$ -physics input including branching ratios  $\mathcal{B}$  and angular observables with the dilepton mass  $q^2$ -range if applicable.

Process	WET	Tree-Level	Loop-Level
$b \rightarrow s\gamma$	$C_7, \{C_8\}$		$\tilde{C}_{uB}, \tilde{C}_{uW}, \{\tilde{C}_{uG}\}, \tilde{C}_{\varphi q}^{(1)}, \tilde{C}_{\varphi q}^{(3)}$
$b \rightarrow s\ell^+\ell^-$	$C_7, \{C_8\}, C_9, C_{10}$	$\tilde{C}_{\varphi q}^+, \tilde{C}_{lq}^+, \tilde{C}_{qe}$	$\tilde{C}_{uB}, \tilde{C}_{uW}, \{\tilde{C}_{uG}\}, \tilde{C}_{\varphi u}, \tilde{C}_{\varphi q}^{(1)}, \tilde{C}_{\varphi q}^{(3)}$ $\tilde{C}_{lu}, \tilde{C}_{eu}, \tilde{C}_{qe}, \tilde{C}_{lq}^{(1)}, \tilde{C}_{lq}^{(3)}$
$b \rightarrow s\nu\bar{\nu}$	$C_L$	$\tilde{C}_{\varphi q}^+, \tilde{C}_{lq}^-$	$\tilde{C}_{uW}, \tilde{C}_{\varphi u}, \tilde{C}_{\varphi q}^{(1)}, \tilde{C}_{\varphi q}^{(3)}$ $\tilde{C}_{lu}, \tilde{C}_{lq}^{(1)}, \tilde{C}_{lq}^{(3)}$
$B_s - \bar{B}_s$ mixing	$C_{V,LL}^{\text{mix}}$		$\tilde{C}_{uW}, \tilde{C}_{\varphi q}^{(1)}, \tilde{C}_{\varphi q}^{(3)}$

TABLE IV: Sensitivities of  $B$ -physics processes to WET and SMEFT Wilson coefficients. The contributions marked as  $\{\tilde{C}_i\}$  are induced by the RGE running in SMEFT and WET at  $\mathcal{O}(\alpha_s)$  only.

### E. $B$ meson decays into neutrinos

While the  $b \rightarrow s\ell^+\ell^-$  FCNCs predominantly probe  $\tilde{C}_{lq}^+$ , the corresponding dineutrino processes  $b \rightarrow s\nu\bar{\nu}$  probes  $\tilde{C}_{lq}^-$ . A combination of both processes is thus crucial to disentangle the singlet and triplet Wilson coefficients and to resolve this otherwise flat direction in a fit of  $b \rightarrow s$  flavor observables. Searches for  $b \rightarrow s\nu\bar{\nu}$  transitions have not yielded an observation. Present 90 % CL upper limits on the  $B^0 \rightarrow K^{*0}\nu\bar{\nu}$  and  $B^+ \rightarrow K^+\nu\bar{\nu}$  branching ratios read [81, 82]

$$\mathcal{B}(B^0 \rightarrow K^{*0}\nu\bar{\nu})_{\text{exp}} < 1.8 \cdot 10^{-5}, \quad \mathcal{B}(B^+ \rightarrow K^+\nu\bar{\nu})_{\text{exp}} < 1.6 \cdot 10^{-5}. \quad (40)$$

The SM and SMEFT predictions can be computed with the effective Lagrangian given in Eq. (2). Within the MFV approach, only the left handed operator  $Q_L$  in Eq. (3) contributes to the  $b \rightarrow s\nu\bar{\nu}$  process while right-handed currents are absent. The branching ratios are thus proportional to the Wilson coefficient  $|C_L|^2$ , the CKM factor  $|V_{tb}V_{ts}^*|^2$  and to the integral over the form factors multiplied by a known  $q^2$ -dependent function. We compute the SM predictions for the branching ratios following [83], using  $|V_{tb}V_{ts}^*| = (41.3 \pm 0.8) \times 10^{-3}$  [84] and  $C_L^{\text{SM}} = -6.32 \pm 0.07$  [85] as numerical inputs. For the  $B \rightarrow K^*$  form factors, we employ the results of Ref. [66], while the  $B \rightarrow K$  form factors are discussed in more detail in App. VII D. For the SM-predictions, we obtain

$$\begin{aligned} \mathcal{B}(B^0 \rightarrow K^{*0}\nu\bar{\nu})_{\text{SM}} &= (8.4 \pm 1.1) \cdot 10^{-6}, \\ \mathcal{B}(B^+ \rightarrow K^+\nu\bar{\nu})_{\text{SM}} &= (4.34 \pm 0.23) \cdot 10^{-6}. \end{aligned} \quad (41)$$

For charged  $B$ -mesons a background from tau-leptons via tree-level decays  $B^+ \rightarrow \tau^+(\rightarrow K^+\nu)\bar{\nu}$  exists that constitutes an additional contribution of  $\mathcal{O}(10\%)$  [86], and needs to be considered in the experimental extraction of the FCNC branching ratio.

New results and the first observation of these branching ratios are expected from the Belle II experiment in the near future, with a predicted precision of roughly 30% [87]. These results will provide important input for global fits and give further insights into possible NP contributions in  $b \rightarrow s$  FCNCs.

To investigate the impact of these future measurements, we perform fits for three different benchmark scenarios. In the SM scenario, we assume SM-like branching ratios for  $\mathcal{B}(B^0 \rightarrow K^{*0} \nu \bar{\nu})$  and  $\mathcal{B}(B^+ \rightarrow K^+ \nu \bar{\nu})$  with an experimental uncertainty of 26% and 30%, respectively, as presumed in Ref. [87]. This corresponds to a hypothetical benchmark "BM SM" measurement of

$$\mathcal{B}(B^0 \rightarrow K^{*0} \nu \bar{\nu})_{\text{BM SM}} = (8.4 \pm 2.2) \cdot 10^{-6}, \quad \mathcal{B}(B^+ \rightarrow K^+ \nu \bar{\nu})_{\text{BM SM}} = (4.3 \pm 1.3) \cdot 10^{-6}. \quad (42)$$

Moreover, we employ two benchmark scenarios with a simultaneous deviation of  $2\sigma$  in both branching ratios to investigate the implications of a possible anomalous measurement. We consider the perspective of enhanced branching ratios by a  $2\sigma$  amplification in both modes "BM +  $2\sigma$ "

$$\mathcal{B}(B^0 \rightarrow K^{*0} \nu \bar{\nu})_{\text{BM}+2\sigma} = (12.7 \pm 2.2) \cdot 10^{-6}, \quad \mathcal{B}(B^+ \rightarrow K^+ \nu \bar{\nu})_{\text{BM}+2\sigma} = (7.0 \pm 1.3) \cdot 10^{-6}, \quad (43)$$

as well as with decreased branching ratios by reducing the signals by  $2\sigma$  "BM -  $2\sigma$ "

$$\mathcal{B}(B^0 \rightarrow K^{*0} \nu \bar{\nu})_{\text{BM}-2\sigma} = (4.0 \pm 2.2) \cdot 10^{-6}, \quad \mathcal{B}(B^+ \rightarrow K^+ \nu \bar{\nu})_{\text{BM}-2\sigma} = (1.7 \pm 1.3) \cdot 10^{-6}. \quad (44)$$

The EFT contributions to the branching ratios in WET are computed with the `flavio` [64] package.

## V. FITS TO DATA

We use a fit procedure analogous to Refs. [4, 13, 38] for which we employ a Bayesian approach as implemented in `EFTfitter` [88], based on `BAT.jl` [89]. All uncertainties are assumed to be Gaussian distributed and correlations are included as far as they are provided. We include systematic and statistical uncertainties of the experimental measurements as well as theory uncertainties arising in the computation of the SM prediction, whereas the theory uncertainties of the BSM corrections are neglected. The EFT contributions are implemented using the parameterization given in Eq. (33). We further employ the MFV-parameterization as described in Sec. III and allow all Wilson coefficients contributing to a given set of observables to be present simultaneously. We assume a flat prior distribution for the SMEFT Wilson coefficients as well as for the MFV ratios  $\gamma_a$  and  $\gamma_b$  in the global fit.

For the fits to the individual sectors, we chose a fixed value for  $\gamma_a$  and  $\gamma_b$  in order to reduce the degrees of freedom and to ensure convergence of the fit. We recall that while  $\gamma_a = 0$  would decouple

the  $b \rightarrow s$  sector,  $\gamma_a = -1$  would lead to the decoupling of the top-quark sector so that both of these values are unsuitable as representative benchmarks. Instead, we set  $\gamma_{a,b} = 1$  in all fits of individual sectors, as this value provides a natural scale for the  $b \rightarrow s$  transitions that are directly proportional to  $\gamma_a$ . Moreover, when neglecting the flavor-diagonal terms, this is the benchmark that directly corresponds to the top-philic approach employed in [13], allowing for a better comparison of the results. Note that  $\gamma_{a,b} = 1$  gives an additional prefactor for some of the Wilson coefficients depending on the flavor, which is important when comparing our results to the literature. For instance, the left-handed down-type couplings for the quark combination  $\bar{d}_{L_i} d_{L_i}$  receive a factor  $(\gamma_a + |V_{ti}|^2)$  compared to a flavor-universal approach, as stated in Eq. (20). This results in a factor  $(1 + |V_{ti}|^2)$  for  $\gamma_a = 1$ . Similarly, the top-quark Wilson coefficients are scaled by a factor of 2 in this setting, following from the factor  $(\gamma_{a,b} + 1)$  in Eqs. (28) and (30). The light up-type and all right-handed down-type Wilson coefficients are unaffected by the MFV ratios  $\gamma_a$  and  $\gamma_b$ .

In Sec. V A, we compare the results derived from the updated top-quark measurements to those obtained from the data analyzed in Ref. [13] utilizing fits of the top sector only. Moreover, we conduct a dedicated analysis of the Drell-Yan production processes in Sec. V B including both, flavor-specific fits of the Drell-Yan measurements as well as an analysis within the MFV framework. The results of the global MFV fit are presented in Sec. V C. In Section V D we analyze the impact of hypothetical measurements of the dineutrino branching ratios on the global fit. Conversely, we use global fit results to predict the  $b \rightarrow s$  dineutrino branching ratios in MFV in Sec. V E.

### A. Updated Fit of the top-quark sector

Compared to the data used in Ref. [13], we employ updated measurements for all observables in the top-quark sector. In addition, we extend the set of observables to encompass the cross sections for the associated production of a top-quark pair with a Higgs boson,  $t\bar{t}H$ , as well as the associated production of a  $W$  boson and a top-quark pair,  $t\bar{t}W$ . A further improvement arises from the differential  $t\bar{t}$ ,  $t\bar{t}Z$  and  $t\bar{t}\gamma$  cross sections, which add a large number of measurements through the multitude of bins. The results of this updated fit compared to the previous one from Ref. [13] are presented in Fig. 3. We give the 90% credible intervals in Tab. V.

Especially the bounds on  $\tilde{C}_{uG}$  are significantly improved in the updated fit due to the inclusion of various differential observables that add a multitude of measurements sensitive to this operator. Moreover, one observes improved bounds on  $\tilde{C}_{uB}$  and  $\tilde{C}_{uW}$  due to the differential  $t\bar{t}\gamma$  and  $t\bar{t}Z$  cross section. The latter also slightly improves the bounds on the penguin operators  $\tilde{C}_{\varphi u}$ ,  $\tilde{C}_{\varphi q}^{(1)}$  and

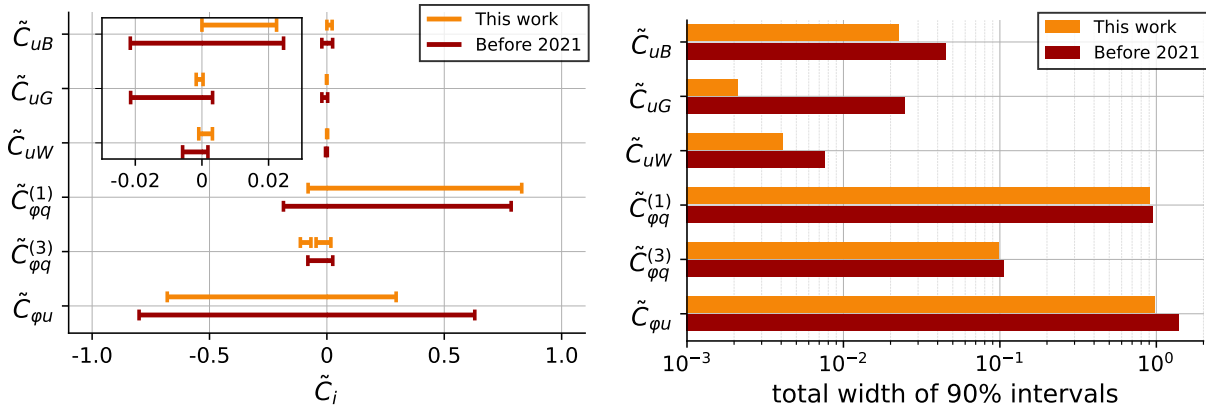


FIG. 3: Constraints on the SMEFT Wilson coefficients  $\tilde{C}_i$  from the top-quark measurements included in Ref. [13] (Before 2021) and from the updated data set listed in Tab. I (This work) assuming  $\Lambda = 10$  TeV and  $\gamma_{a,b} = 1$ . Shown are the 90% credible intervals (left) and the total width of these intervals (right).

$\tilde{C}_{\varphi q}^{(3)}$ . The triplet coupling  $\tilde{C}_{\varphi q}^{(3)}$  as well as  $\tilde{C}_{uW}$  are moreover probed by the top-quark width  $\Gamma_t$ , for which the experimental uncertainties have decreased. Similarly, the experimental precision of the measurement of the helicity fractions  $f_0$  and  $f_L$  has also been improved, which further tightens the limits on  $\tilde{C}_{uW}$ .

### B. Fit of Drell-Yan observables

In order to assess the impact of the Drell-Yan measurements on the global fit, we conduct an analysis including only the Drell-Yan observables using the MFV framework described in Sec. III. We consider all SMEFT operators except for the dipoles, whose contributions to Drell-Yan production vanish due to neglecting the light Yukawa couplings in our setup (19). The fit is performed assuming  $\Lambda = 10$  TeV to ensure the validity of the EFT framework. We employ all measurements listed in

	$\tilde{C}_{uB}$	$\tilde{C}_{uG}$	$\tilde{C}_{uW}$
Before 2021	[-0.0215, 0.0245]	[-0.0214, 0.0032]	[-0.0058, 0.0018]
This work	[-0.000, 0.0224]	[-0.0017, 0.0003]	[-0.0010, 0.0032]
	$\tilde{C}_{\varphi q}^{(1)}$	$\tilde{C}_{\varphi q}^{(3)}$	$\tilde{C}_{\varphi u}$
Before 2021	[-0.19, 0.99]	[-0.081, 0.025]	[-0.80, 0.63]
This work	[-0.08, 0.83]	[-0.113, 0.017]	[-0.68, 0.30]

TABLE V: 90% credible intervals of the top-quark fits employing the measurements included in Ref. [13] (Before 2021) and from the updated data set listed in Tab. I (This work). We use  $\Lambda = 10$  TeV and  $\gamma_{a,b} = 1$ .

Tab. II and fit all 11 coefficients simultaneously while setting  $\gamma_{a,b} = 1$ . In addition, we perform separated fits including only the NC or the CC measurements. In the CC fit, only the triplet Wilson coefficients  $\tilde{C}_{\varphi q}^{(3)}$  and  $\tilde{C}_{lq}^{(3)}$  are considered as degree of freedom, since all other operators are insensitive to this process. The results are presented in Fig. 4, showing the 90% credible intervals as well as the total width of these intervals. The 90% credible intervals are furthermore listed in Tab. VI.

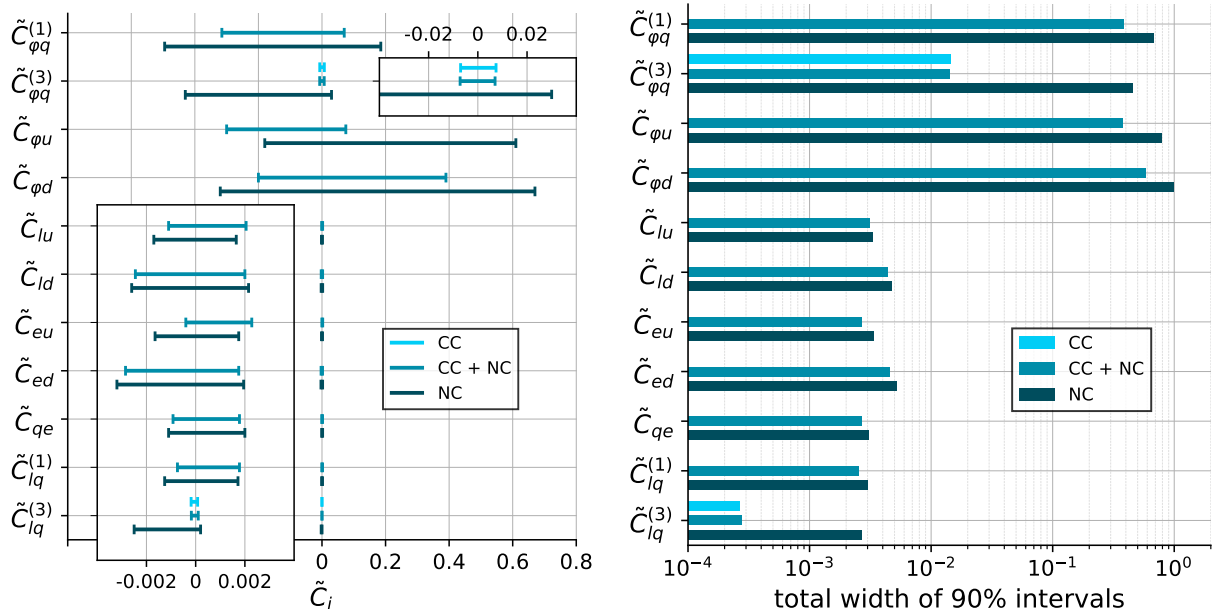


FIG. 4: Constraints on the SMEFT Wilson coefficients  $\tilde{C}_i$  from the Drell-Yan measurements presented in Tab. II assuming  $\Lambda = 10$  TeV and  $\gamma_a = 1$ . Shown are the 90% credible intervals (left) and the total width of these intervals (right).

Our study shows that the four-fermion operators can be potentially constrained by the Drell-Yan measurements, with bounds of the order  $10^{-3}$  within the MFV framework. The limits on the penguin operators, in contrast, are approximately two orders of magnitude inferior with widths of the order  $10^{-1}$  to  $10^0$ . This difference between the two types of operators is consistent with the different scaling with energy. The triplet operators  $\tilde{C}_{\varphi q}^{(3)}$  and  $\tilde{C}_{lq}^{(3)}$  are especially well constrained since they contribute to the CC Drell-Yan process exclusively.

In addition to the Drell-Yan fit within the MFV framework, we furthermore conduct flavor-specific fits with regard to the lepton as well as to the quark flavor in order to investigate the impact of the different flavor compositions. Again, we impose the benchmark  $\gamma_a = 1$  and allow all Wilson coefficients of a given quark flavor combination to be present simultaneously. Following from the MFV parameterization outlined in Sec. III C, we assume no lepton-flavor violating contributions. This is particularly relevant for the CC process, as it involves neutrinos whose flavor cannot be

Coefficient	NC + CC	NC	CC
$\tilde{C}_{\varphi q}^{(1)}$	[-0.315, 0.07]	[-0.495, 0.185]	
$\tilde{C}_{\varphi q}^{(3)}$	[-0.0072, 0.007]	[-0.43, 0.03]	[-0.007, 0.0074]
$\tilde{C}_{\varphi u}$	[-0.3, 0.075]	[-0.18, 0.61]	
$\tilde{C}_{\varphi d}$	[-0.2, 0.39]	[-0.32, 0.67]	
$\tilde{C}_{lu}$	[-0.0011, 0.002]	[-0.0017, 0.0016]	
$\tilde{C}_{ld}$	[-0.0024, 0.002]	[-0.0026, 0.0021]	
$\tilde{C}_{eu}$	[-0.0004, 0.0023]	[-0.0016, 0.0018]	
$\tilde{C}_{ed}$	[-0.0028, 0.0017]	[-0.0032, 0.0019]	
$\tilde{C}_{qe}$	[-0.0009, 0.0018]	[-0.0011, 0.002]	
$\tilde{C}_{lq}^{(1)}$	[-0.0007, 0.0018]	[-0.0013, 0.0017]	
$\tilde{C}_{lq}^{(3)}$	[-0.0002, 0.0001]	[-0.0025, 0.0002]	[-0.0002, 0.0001]

TABLE VI: 90% credible limits of the Drell-Yan fits within MFV. We use  $\Lambda = 10$  TeV and  $\gamma_a = 1$ .

determined experimentally. The 90% credible intervals of the flavor-diagonal NC and the CC process are shown in Figs. 5 and 6, respectively, and in Tabs. VIII–XI in the appendix VII C.

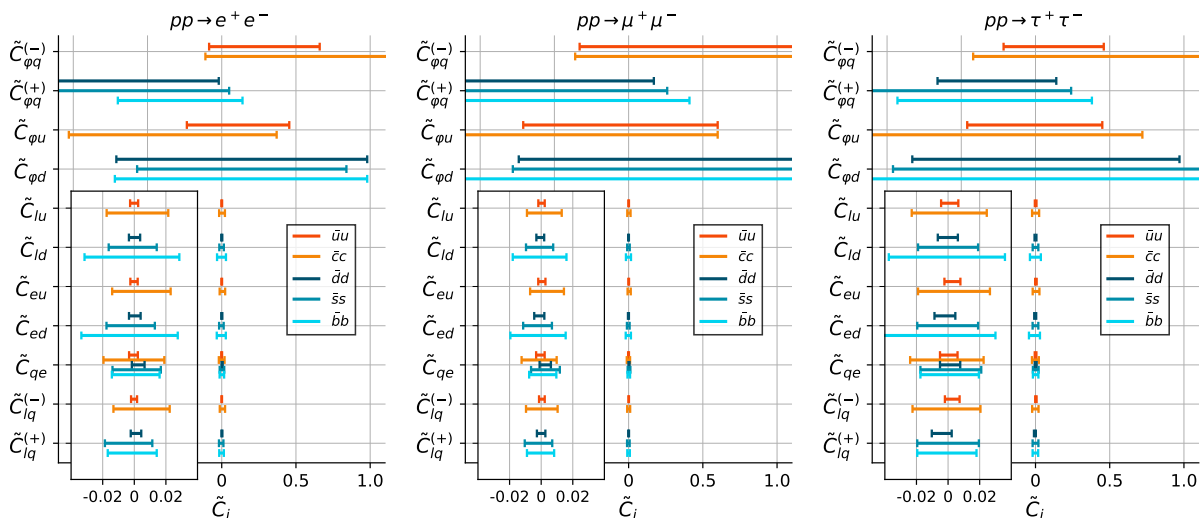


FIG. 5: Flavor-specific constraints on the SMEFT Wilson coefficients  $\tilde{C}_i$  from the NC Drell-Yan measurements presented in Tab. II assuming  $\Lambda = 10$  TeV and  $\gamma_{a/b} = 1$ . Shown are the 90% credible intervals for  $pp \rightarrow e^+e^-$  (left),  $pp \rightarrow \mu^+\mu^-$  (middle) and  $pp \rightarrow \tau^+\tau^-$  (right).

We also perform fits of the FCNC quark combinations  $ds$ ,  $db$  and  $sb$ , for which the bounds are, however, several orders of magnitude larger due to the CKM suppression arising in the MFV framework. Therefore, we do not show the limits of the FCNC processes in the plots, but give the ranges in the appendix in Tab. XII.



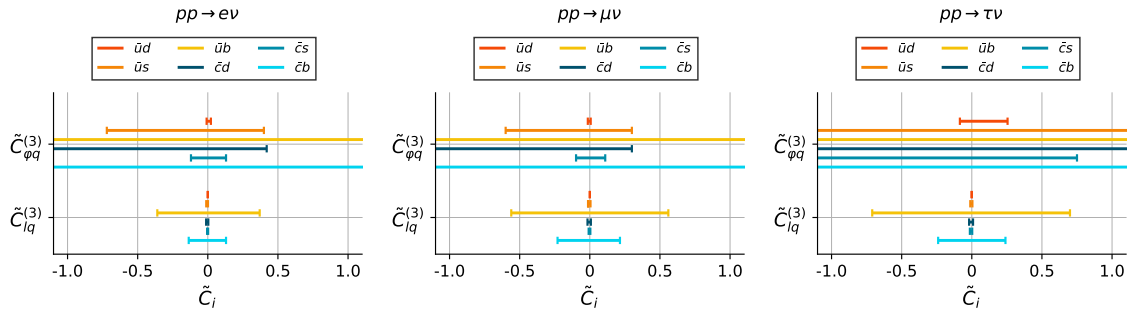


FIG. 6: Flavor-specific constraints on the SMEFT Wilson coefficients  $\tilde{C}_i$  from the CC Drell-Yan measurements presented in Tab. II assuming  $\Lambda = 10$  TeV and  $\gamma_{a/b} = 1$ . Shown are the 90% credible intervals for  $pp \rightarrow e\nu$  (left),  $pp \rightarrow \mu\nu$  (middle) and  $pp \rightarrow \tau\nu$  (right).

The strongest individual constraint arises from the CC  $pp \rightarrow \mu\nu$  process for the Wilson coefficient  $\tilde{C}_{lq}^{(3)}$  with a 90% credible interval of  $[-0.0001, 0.0003]$  for the  $ud$  quark flavor combination. In general, the constraints on the Wilson coefficients arising from the measurements including muons are slightly better than the ones obtained from electron or tau lepton measurements, due to the differences in the detection and reconstruction efficiency. Regarding the quark flavor, the best limits are found for up and down quark as expected from the parton-parton luminosities shown in Fig. 1. In contrast, flavor combinations involving  $b$  quarks are the least well constrained. We find that our bounds are consistent with the limits derived in Ref. [22].

The MFV fit improves the bounds on the Wilson coefficients in comparison to the flavor-specific fits, since it combines all flavor-specific limits. Specifically, each lepton flavor couples universally and all quark combinations contribute simultaneously to a given Wilson coefficient, resulting in an enhancement of the bounds on the Wilson coefficients. These findings demonstrate that the Drell-Yan observables are a powerful tool to constrain the Wilson coefficients within the MFV scenario. This is especially pronounced for the four-fermion operators, which further profit from the energy enhancement present in the high- $p_T$  tails of the distributions.

### C. Global analysis

We perform a global fit of all sectors, beauty,  $Z$ , top and Drell-Yan, in order to investigate and exploit the synergies arising in the combination of the different types of observables. The resulting bounds on the Wilson coefficients are presented in Fig. 7 and the 90% credible limits are listed in Tab. VII. We compare the results of this global fit to analyses of the individual sectors in which we set  $\gamma_{a,b}=1$  and include only the Wilson coefficients contributing to the respective sector

as degrees of freedom. The  $b \rightarrow s$  measurements are fitted together with the  $Z$  observables in order to ensure the convergence of the fit, which is otherwise difficult to achieve due to the high number of contributing Wilson coefficients in the matching at the one-loop level. In the  $b \rightarrow s$  and  $Z$  fit, there is no sensitivity to  $\tilde{C}_{lq}^{(1)}$  and  $\tilde{C}_{lq}^{(3)}$ , but only on their linear combination  $\tilde{C}_{lq}^+$ . Therefore, we constrain  $\tilde{C}_{lq}^+$  instead of the individual Wilson coefficients in this fit.

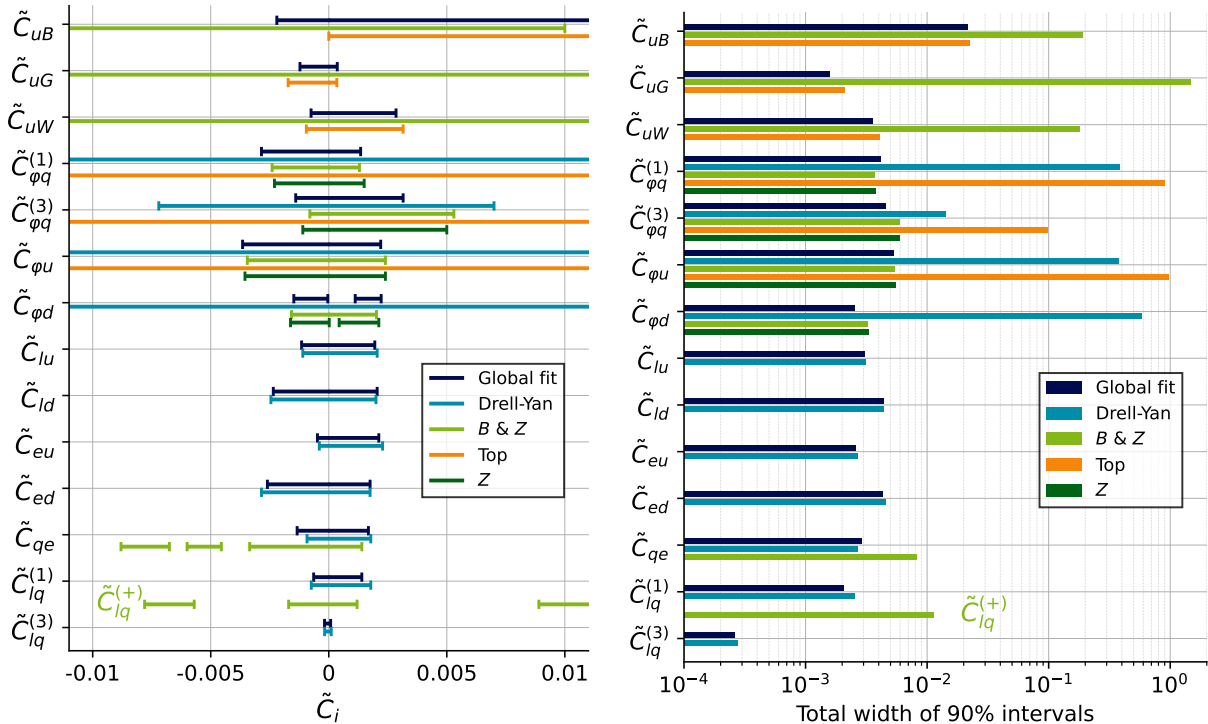


FIG. 7: Constraints on the SMEFT Wilson coefficients  $\tilde{C}_i$  assuming  $\Lambda = 10$  TeV and a flat prior in the range  $[-1, 1]$  for  $\tilde{C}_i$ . Shown are the 90% credible intervals (left) and the total width of these intervals (right). We compare the result of the global fit including top,  $B$ -physics,  $Z$ -decay and Drell-Yan measurements to the fit results of the individual sectors. For the global fit, we simultaneously fit  $\gamma_{a,b}$  with a flat prior in the range  $-10 \leq \gamma_{a,b} \leq 10$ , whereas this parameter is set to  $\gamma_{a,b}=1$  for the individual fits. In the  $B + Z$  fit, we can only constrain  $C_{lq}^+$ . See text for details.

Our findings demonstrate that the combination of the various sectors leads to synergies that improve the bounds on the Wilson coefficients. This is especially pronounced for  $\tilde{C}_{uG}$ ,  $\tilde{C}_{\phi q}^{(3)}$ ,  $\tilde{C}_{\phi d}$  and  $\tilde{C}_{lq}^{(1)}$ . For other Wilson coefficients, in particular  $\tilde{C}_{\phi q}^{(1)}$  and  $\tilde{C}_{qe}$ , the limits of the combined fit are slightly inferior to the bounds derived from the individual sectors. This results from the increased number of degrees of freedom in the global fit in comparison to the analyses of the individual sectors, for example the  $Z$ -fit which comprises only four free parameters. Moreover, the 90% credible interval of  $\tilde{C}_{\phi q}^{(1)}$  in the top-quark fit is slightly shifted with regard to the results from

Coefficient	Global Fit ( $\cdot 10^3$ )	Drell-Yan ( $\cdot 10^3$ )	$B$ and $Z$ ( $\cdot 10^3$ )	Top ( $\cdot 10^3$ )	$Z$ ( $\cdot 10^3$ )
$\tilde{C}_{uB}$	[-2.2, 19.6]		[-700, -665] [-635, -575] [-120, -75] [-40, 10]	[0.0, 22.4]	
$\tilde{C}_{uG}$	[-1.22, 0.36]		[-1000, 990]	[-1.72, 0.34]	
$\tilde{C}_{uW}$	[-0.75, 2.9]		[-105, 55]	[-0.95, 3.15]	
$\tilde{C}_{\varphi q}^{(1)}$	[-2.9, 1.3]	[-315, 70]	[-2.4, 1.3]	[-80, 830]	[-2.3, 1.5]
$\tilde{C}_{\varphi q}^{(3)}$	[-1.4, 3.2]	[-7.2, 7.0]	[-0.8, 5.3]	[-113, -98] [-88, -68] [-46, 17]	[-1.1, 5.0]
$\tilde{C}_{\varphi u}$	[-3.65, 2.20]	[-300, 75]	[-3.5, 2.4]	[-680, 295]	[-3.6, 2.4]
$\tilde{C}_{\varphi d}$	[-1.48, -0.040] [1.12, 2.22]	[-200, 390]	[-1.58, 2.02]		[1.62, 0.02] [0.44, 2.12]
$\tilde{C}_{lu}$	[-1.15, 1.95]	[-1.1, 2.0]			
$\tilde{C}_{ld}$	[-2.35, 2.05]	[-2.45, 2.0]			
$\tilde{C}_{eu}$	[-0.48, 2.12]	[-0.40, 2.28]			
$\tilde{C}_{ed}$	[-2.6, 1.75]	[-2.85, 1.75]			
$\tilde{C}_{qe}$	[-1.34, 1.68]	[-0.92, 1.78]	[-8.8, -6.8] [-6.0, -4.6] [-3.4, 1.4]		
$\tilde{C}_{lq}^{(1/+)}$	[-0.64, 1.4]	[-0.74, 1.78]	[-7.8, -5.7] [-1.7, 1.2] [8.9, 11.5]		
$\tilde{C}_{lq}^{(3)}$	[-0.18, 0.08]	[-0.17, 0.11]			

TABLE VII: 90% credible intervals multiplied by  $10^3$  of the global MFV Fit as well as the fits of the individual sectors. The fits are performed assuming  $\Lambda = 10$  TeV and a flat prior in the range  $[-1, 1]$  for all Wilson coefficients  $\tilde{C}_i$ . In the global fit,  $\gamma_{a,b}$  are included as degrees of freedom whereas we set them to  $\gamma_{a,b} = 1$  in the fits to individual sectors. In the  $B + Z$  fit, we can only constrain  $C_{lq}^+$ . See text for details.

the other fits. This leads to a widening of the 90% credible interval in the combined fit.

Furthermore, the limits on the four-fermion operators are strongly dominated by the Drell-Yan measurements as expected from their energy enhancement and the results presented in Sec. VB. The penguin operators, on the other hand, are predominantly constrained by the  $Z$  observables while the dipole operators receive the strongest bounds from the top-quark sector. The Wilson coefficient that is best constrained is  $\tilde{C}_{lq}^{(3)}$  with a 90% credible interval of  $[-1.8 \cdot 10^{-4}, 0.8 \cdot 10^{-4}]$ , resulting from the strong bounds due to the NC as well as especially the CC Drell-Yan process.

The global fit also probes the MFV parameters  $\gamma_a$  and  $\gamma_b$  defined in Eqs. (29), (31). The one-dimensional marginalized posterior probability distributions of these two parameters are presented in Fig. 8.

Our results indicate that the fit is not very sensitive to  $\gamma_b$ . This parameter is probed by the

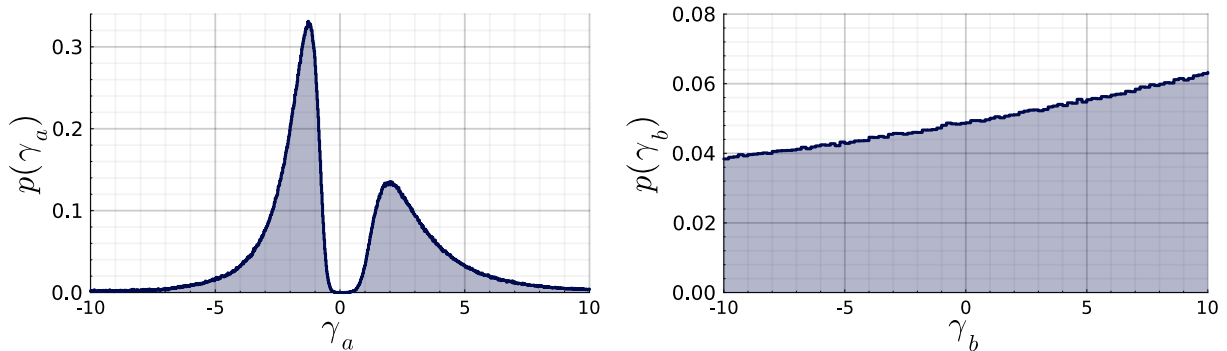


FIG. 8: Marginalized posterior probability distributions of the MFV parameters  $\gamma_a$  and  $\gamma_b$  defined in Eqs. (29), (31) for  $\Lambda = 10$  TeV obtained from the global fit including top,  $B$ -physics,  $Z$ -decay and Drell-Yan measurements. We choose a uniform distribution in the interval  $-10 \leq \gamma_{a,b} \leq 10$  as the prior probability distribution.

interplay of the Drell-Yan and  $Z \rightarrow c\bar{c}$  observables on the one hand, together with the top-quark limits and the one-loop contributions to the  $b \rightarrow s$  transitions on the other hand. While the former constrains NP contributions to the light up-type quarks and thus to  $\tilde{C}_{u\bar{u}}$ , the latter tests top-quark transitions and hence the linear combination  $\tilde{C}_{u\bar{u}}(1 + \gamma_b)$ . The bounds on  $\tilde{C}_{u\bar{u}}(1 + \gamma_b)$  are, however, significantly smaller than the bounds on  $\tilde{C}_{u\bar{u}}$ , so that there is only a minor sensitivity on  $\gamma_b$ . The parameter  $\gamma_a$ , in contrast, shows a distinct double-peak behaviour with a large peak at roughly  $\gamma_a = -1.2$  and a smaller peak at  $\gamma_a = 1.9$ . The posterior probability distribution further features a minimum around  $\gamma_a = 0$ .

These findings indicate that the second order of the MFV expansion for left-handed quarks is favored to have a slightly larger absolute value compared to the leading, flavor diagonal term of the MFV expansion. Higher order terms at order one have also been noted in [12, 90]. In case of the maximum near  $\gamma_a = -1.2$ , both terms conspire to cancel each other in part in the top quark coupling given in Eq. (20), which is proportional to  $1 + \gamma_a$ .

The minimum at  $\gamma_a = 0$  is caused by the anomalies in the  $b \rightarrow s\mu\mu$  observables, such as the  $B^0 \rightarrow K^{*0}\mu^+\mu^-$  decay distributions measured by LHCb which exhibit a tension with the SM predictions at approximately  $3\sigma$  [76]. These  $b \rightarrow s$  observables are directly proportional to  $\gamma_a$  multiplied by the Wilson coefficient; for details see Sec. III C. Since the Wilson coefficients are already tightly constrained by the Drell-Yan and top-quark measurements that are in good agreement with the SM predictions, the parameter  $\gamma_a$  is pushed towards larger values to account for the deviations of the  $B$ -measurements from the SM predictions.

To support this hypothesis, we repeat the global fit setting all  $B$ -physics measurements to their

SM prediction while keeping the uncertainties. The results of the marginalized one-dimensional posterior probability distributions of  $\gamma_a$  are shown in the left panel of Fig. 9. The value  $\gamma_a = 0$

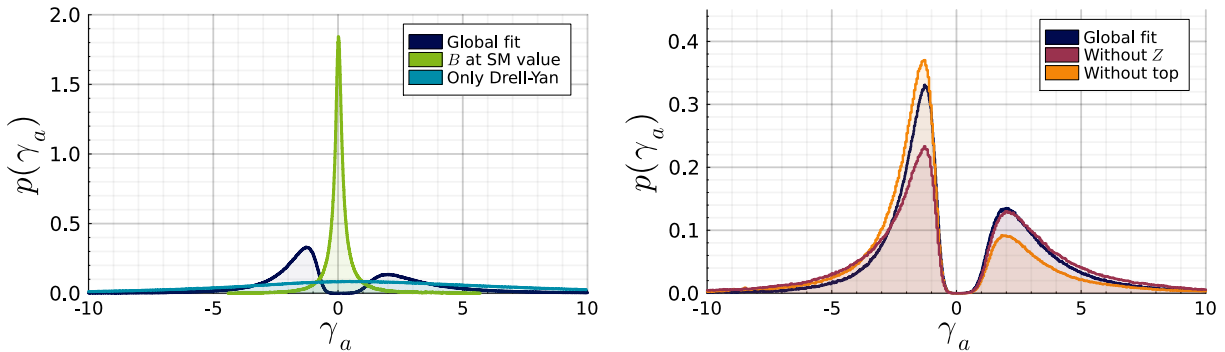


FIG. 9: Impact of the  $b \rightarrow s$  anomalies and other sectors on the marginalized posterior distribution of  $\gamma_a$ . In the left panel we compare the global MFV fit (dark blue) to a scenario in which all  $b \rightarrow s$  measurements are set to their SM prediction while keeping uncertainties unchanged (green). We also show the distribution from a pure Drell-Yan fit (light blue). In the right panel we show the global fit (dark blue) and fits excluding all top-quark observables (orange) and one excluding the  $Z$  observables (red). All fits are performed assuming  $\Lambda = 10$  TeV.

is favored in the scenario with  $B$ -data at SM values (green), supporting the hypothesis that the anomalies present in the  $b \rightarrow s$  FCNCs are responsible for the minimum at  $\gamma_a = 0$  in the global fit (dark blue). For comparison, we also show  $p(\gamma_a)$  using Drell-Yan data only (light blue). We learn that the latter are consistent with a wide range of  $\gamma_a$ , with a maximum at zero, as expected since the Drell-Yan data are in agreement with the SM predictions.

To further investigate the impact of the different sectors on the MFV parameters, we repeat the global fit and separately exclude the  $Z$  (red), or the top (orange) measurements from the fit, shown in the right panel of Fig. 9. We learn that neither the  $Z$  nor the top data alone are central to deciphering the flavor structure. However, excluding the  $t\bar{t}$ -observables significantly loosens bounds on the dipole operators, whereas removing the  $Z$ -pole data decreases the sensitivity to the penguins.

#### D. Impact of dineutrino measurements on the global fit

We perform the global fit including the hypothetical benchmark measurements of the  $B^0 \rightarrow K^{*0} \nu \bar{\nu}$  and  $B^+ \rightarrow K^+ \nu \bar{\nu}$  branching ratios detailed in Sec. IV E. The resulting 90% credible intervals of the Wilson coefficients are shown in Fig. 10 and the marginalized one-dimensional posterior probability distributions of  $\gamma_a$  in Fig. 11.

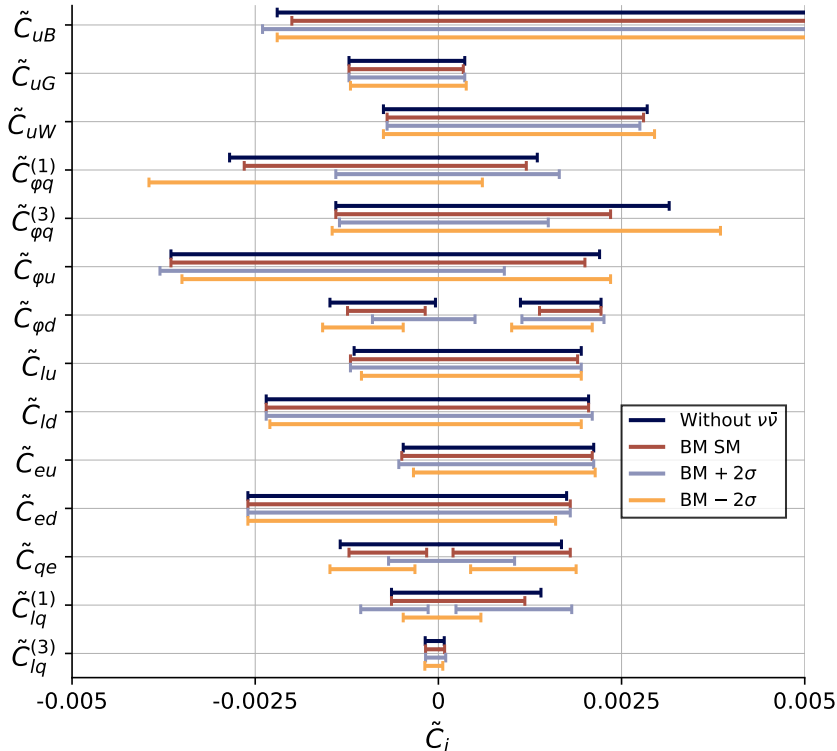


FIG. 10: Impact of hypothetical benchmark measurements of the branching ratios  $B^0 \rightarrow K^{*0}\nu\bar{\nu}$  and  $B^+ \rightarrow K^+\nu\bar{\nu}$  on the 90% credible intervals of the SMEFT Wilson coefficients in the global MFV fit. We compare the results from the global fit without  $b \rightarrow s\nu\bar{\nu}$  observables to the fits including a hypothetical SM-like measurement (BM SM) (42), a benchmark with a  $2\sigma$  excess (BM  $+2\sigma$ ) (43) and a benchmark with a  $2\sigma$  decrease (BM  $-2\sigma$ ) (44) in the branching ratios. All fits are performed assuming  $\Lambda = 10$  TeV and a flat prior in the range  $-10 \leq \gamma_{a,b} \leq 10$ .

We learn that the hypothetical dineutrino benchmarks have a significant impact on the Wilson coefficients, particularly on the penguin operators as well as the four-fermion operators with left-handed quarks, see Fig. 10. A measurement with the expected sensitivity of Belle II can signal NP in the SMEFT coefficients  $\tilde{C}_{\phi d}$ ,  $\tilde{C}_{qe}$  or  $\tilde{C}_{lq}^{(1)}$ . Notably, even a SM-like measurement would imply a deviation in  $\tilde{C}_{qe}$  and  $\tilde{C}_{\phi d}$ , which can be accounted for by the anomalies in the  $b \rightarrow s\ell\bar{\ell}$  observables as well as the persistent tension of the  $Z \rightarrow b\bar{b}$  observables from the SM prediction [91]. A hypothetical measurement with a  $2\sigma$  decrease of the branching ratios would further increase this tension, whereas a measurement with a  $2\sigma$  excess would result in 90% credible intervals for  $\tilde{C}_{qe}$  and  $\tilde{C}_{\phi d}$  compatible with  $\tilde{C}_i = 0$ . In the latter case we would, however, observe a non-zero value for  $\tilde{C}_{lq}^{(1)}$ , which is in agreement with the SM in the other two benchmark scenarios. These findings highlight that a measurement of the dineutrino branching ratio would provide a useful input to the

global fit to disentangle BSM physics.

Our analysis further indicates that a measurement of the dineutrino branching ratios can have a significant impact on the MFV parameter  $\gamma_a$ , especially if a deviation from the SM would be observed, see Fig. 11. Enhanced dineutrino branching ratios would be in line with the fit to current data and yield a similar shape of the posterior probability distribution of  $\gamma_a$ , as shown in the left panel. On the other hand, the benchmarks featuring reduced branching ratios (right panel) show an increase of the height of the second peak favoring positive values of  $\gamma_a$  while the presently favored one at  $\gamma_a \sim -1.2$  is reduced in comparison.

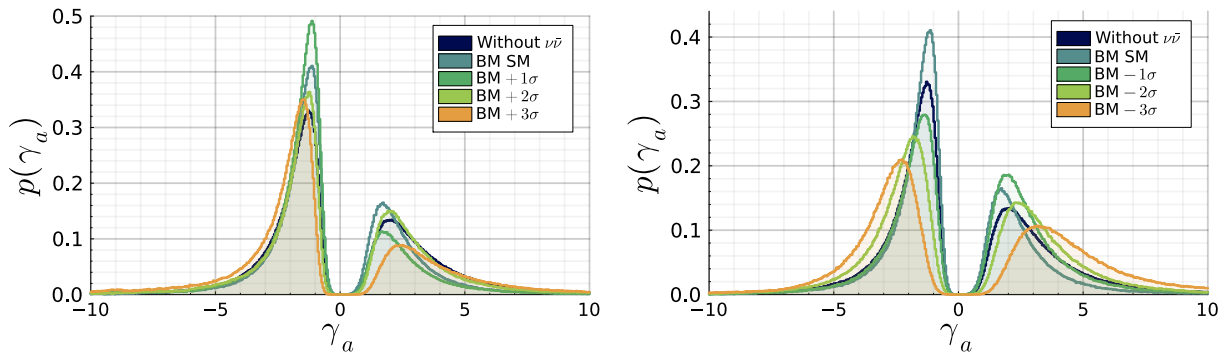


FIG. 11: Impact of hypothetical benchmark measurements of the dineutrino branching ratios  $B^0 \rightarrow K^{*0}\nu\bar{\nu}$  and  $B^+ \rightarrow K^+\nu\bar{\nu}$  on the one-dimensional marginalized posterior probability distribution of  $\gamma_a$ . We compare the results from the global fit without  $b \rightarrow s\nu\bar{\nu}$  observables to the fits including a hypothetical SM-like measurement (BM SM) (42) and benchmarks with enhanced branching ratios (left) as well as to decreased branching ratios (right). All fits are performed assuming  $\Lambda = 10$  TeV and a flat prior for  $\gamma_a$ .

### E. Predictions of dineutrino branching ratios from the global fit

In addition to studying the impact of future measurements of the dineutrino branching ratios on the global fit in Sec. V D, here, we infer predictions on the dineutrino branching ratios from the global fit. We employ the posterior probability distributions obtained in Sec. V C and insert them into the parameterization of the branching ratios derived in Sec. IV E to compute the allowed ranges of  $B \rightarrow K^{(*)}\nu\bar{\nu}$  branching ratios within our MFV setup. The resulting probability distributions are presented in Fig. 12 together with the current experimental upper limits (red) at 90% confidence level [81, 82] and the SM prediction (41) (grey) including its  $1\sigma$  uncertainty.

We obtain the following 68% credible intervals from the MFV-based fit

$$4.25 \cdot 10^{-6} \leq \mathcal{B}(B^0 \rightarrow K^{*0}\nu\bar{\nu}) \leq 11.13 \cdot 10^{-6}, \quad 2.26 \cdot 10^{-6} \leq \mathcal{B}(B^+ \rightarrow K^+\nu\bar{\nu}) \leq 5.78 \cdot 10^{-6}, \quad (45)$$

with corresponding 90% upper limits  $13.13 \cdot 10^{-6}$  and  $6.82 \cdot 10^{-6}$ , respectively, which are below the current experimental limits (40). The dineutrino modes are maximally positive correlated in our setup, since both are affected by a single Wilson coefficient only,  $C_L$  in WET. The corresponding right-handed Wilson coefficient vanishes as we neglect all down-type Yukawas (19). The ratio of branching fractions hence depends only on form factors and meson masses, whereas the CKM elements and the Wilson coefficient cancel. We obtain

$$\frac{\mathcal{B}(B^+ \rightarrow K^+ \nu \bar{\nu})}{\mathcal{B}(B^0 \rightarrow K^{*0} \nu \bar{\nu})} = 0.52 \pm 0.06, \quad (46)$$

which equals the value in the SM [64]. This prediction can be verified experimentally in order to test the leading order MFV hypothesis.

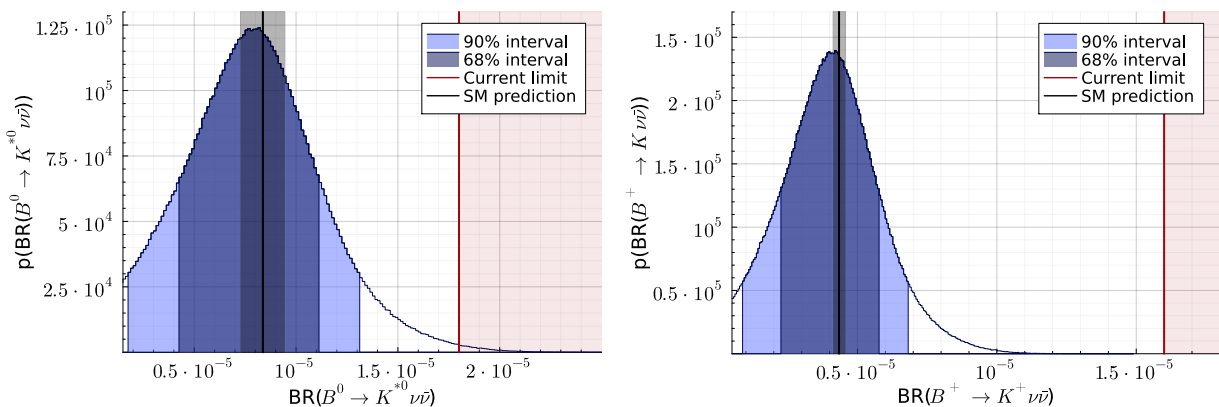


FIG. 12: Marginalized posterior probability distribution of the branching ratios  $\mathcal{B}(B^0 \rightarrow K^{*0} \nu \bar{\nu})$  (left) and  $\mathcal{B}(B^+ \rightarrow K^+ \nu \bar{\nu})$  (right). Shown are the 90% and 68% credible intervals in blue together with the current 90% CL experimental limits (40) in red as well as SM predictions with  $1\sigma$  uncertainty (41) in grey.

We note that the dineutrino branching ratios (45) from our global MFV fit are not significantly altered with respect to their SM values (41). This can be accounted for by the fact that the Wilson coefficients are all compatible with  $\tilde{C}_i = 0$ , corresponding to SM-like measurements. We also note that in simplified NP models with  $C_{lq}^{(1)}$  only, or dominating over  $C_{lq}^{(3)}$ , the dineutrino modes are enhanced relative to the SM as a result of the suppression of the  $b \rightarrow s \mu \mu$  ones [92]. This can be understood from the matching in App. VII A and the fact that leading effects are from SM-NP interference and that the leading SM contributions have opposite sign,  $C_9^{\text{SM}} - C_{10}^{\text{SM}} = +8.2$  and  $C_L^{\text{SM}} = -6.32$ .



## VI. CONCLUSIONS

We perform a global fit of 14 Wilson coefficients of dimension-six SMEFT operators (1) to Beauty, Top,  $Z \rightarrow b\bar{b}, c\bar{c}$  and Drell-Yan measurements. We work within the MFV ansatz, allowing for no further flavor violation than already present in the Standard Model, *i.e.*, due to fermion mixing and masses. In the fit we consider two additional degrees of freedom,  $\gamma_a, \gamma_b$ , (29), (31) arising within MFV from the top quark Yukawa coupling. The term  $\gamma_a$  is required to address the  $B$ -data as neglecting it would switch off BSM contributions to the  $b \rightarrow s$  FCNCs. The term  $\gamma_b$  belongs to the right-handed up-type quark sector and induces non-universality between the top quark and the other generations. The full global fit we perform is hence 16-dimensional.

We obtain constraints from fitting to the individual sectors, beauty plus  $Z$ , top quark and Drell-Yan, and their combination, illustrated in Fig. 7, from where improved constraints in the combination and synergies can be observed. Removing the top quark measurements, bounds on the dipole operators weaken. Removing the  $Z$ -data, bounds on the penguins significantly weaken. The Drell-Yan measurements are a new ingredient over previous works [13], which explored top-bottom synergies with a top-philic flavor pattern, that has only subleading sensitivity to  $pp \rightarrow \ell\ell$  and  $pp \rightarrow \ell\nu$ . Here, using MFV, we find the Drell-Yan constraints to be extremely powerful, as a result of the high multiplicity of contributing channels in this flavor ansatz. We also present lepton-flavor specific limits for neutral and charged currents from quark flavor-specific operators in Figs. 5 and 6, respectively. The strongest bounds in the global fit exist on the semileptonic four-fermion triplet operator  $O_{lq}^{(3)}$ , probing scales as high as 18 TeV, followed by the gluon dipole operator  $O_{uG}$  with 7 TeV, and other four-fermion and penguin operators in the multi-TeV range. The coefficient  $\tilde{C}_{uB}$  remains the most weakly constrained one. Progress can be expected from measurements involving top quarks and photons [93], whose analysis is beyond the scope of this work. The 90 % credible ranges of the global MFV fit are summarized in Table VII.

The FCNC  $b \rightarrow s\mu\mu$  measurements together with the other sectors allow to probe flavor patterns and test the MFV ansatz. The results of the fit point to an order one higher-order contribution in the spurion expansion induced by the top-quark Yukawa coupling,  $\gamma_a \sim -1.2$ , see Fig. 9. This is a sizable correction that hinges on the discrepancies between data on  $b \rightarrow s\mu\mu$  angular distributions and branching ratios and corresponding SM predictions, and requires further scrutiny. The corresponding contribution  $\gamma_b$  from the right-handed up-type quark sector turns out to be poorly constrained, see Fig. 8 (right panel). This can be improved in collider studies with top quarks and leptons at the LHC [94, 95], and future colliders, in  $ee \rightarrow t\bar{t}$  at the FCC-ee [96], or in  $t\bar{t}$  production

at a muon collider [97, 98]. Further future directions for flavorful SMEFT fits include the study of up-quark sector FCNCs, induced by finite down-type Yukawa couplings that switch on other higher order terms of MFV, or an analysis that covers  $b \rightarrow d$  data, which are presently consistent with MFV [99], although within large experimental uncertainties.

The results of the global fit also allows to predict the branching ratios of FCNC dineutrino decays  $B \rightarrow K^{(*)}\nu\bar{\nu}$  decays, for which presently only upper limits, about a factor few higher than the SM predictions, exist. Our predictions (45) include the SM and are in reach of Belle II [87]. We also find that a future measurement of the dineutrino branching ratios provides useful information on the global fit to disentangle BSM physics.

**Note added:** While this paper was under review, Belle II published their first measurement of the  $B^+ \rightarrow K^+\nu\bar{\nu}$  branching ratio at  $2.4 \pm 0.7 \cdot 10^{-5}$  [100], which is enhanced relative to the SM prediction (41) and challenges MFV, see Fig. 12.

### Acknowledgments

We are happy to thank Rigo Bause and Hector Gisbert for useful discussions. LN is supported by the doctoral scholarship program of the *Studienstiftung des Deutschen Volkes*. GH gratefully acknowledges an IPPP DIVA fellowship. This work was supported in part by the Deutsche Forschungsgemeinschaft (DFG) through the PUNCH4NFDI consortium supported by the DFG fund NFDI 39/1.

## VII. AUXILIARY INFORMATION

### A. Analytical Matching

We match the SMEFT onto the WET within the MFV framework introduced in Sec. III. The tree-level matching equations read:

$$\Delta C_9^{\text{tree}} = \frac{\pi}{\alpha} \gamma_a \left[ \tilde{C}_{lq}^+ + \tilde{C}_{qe} + (-1 + 4 \sin^2 \theta_w) \tilde{C}_{\varphi q}^+ \right], \quad (47)$$

$$\Delta C_{10}^{\text{tree}} = \frac{\pi}{\alpha} \gamma_a \left[ -\tilde{C}_{lq}^+ + \tilde{C}_{qe} + \tilde{C}_{\varphi q}^+ \right], \quad (48)$$

$$\Delta C_L^{\text{tree}} = \frac{\pi}{\alpha} \gamma_a \left[ \tilde{C}_{lq}^- + \tilde{C}_{\varphi q}^+ \right]. \quad (49)$$

The one-loop matching equations read [31, 101, 102]:

$$\Delta C_7^{\text{loop}} = \sqrt{2} \frac{m_t}{m_W} \left[ \tilde{C}_{uW} E_7^{uW}(x_t) + \tilde{C}_{uW}^* F_7^{uW}(x_t) + \frac{\cos \theta_w}{\sin \theta_w} \left( \tilde{C}_{uB} E_7^{uB}(x_t) + \tilde{C}_{uB}^* F_7^{uB}(x_t) \right) \right] \\ + \gamma_a \cdot \left( \tilde{C}_{\varphi q}^+ E_7^{\varphi q} + C_{\varphi q}^{(3)} F_7^{\varphi q} \right) + (1 + \gamma_a) \cdot \tilde{C}_{\varphi q}^{(3)} D_0'(x_t), \quad (50)$$

$$\Delta C_8^{\text{loop}} = \sqrt{2} \frac{m_t}{m_W} \left[ \tilde{C}_{uW} E_8^{uW}(x_t) + \tilde{C}_{uW}^* F_8^{uW}(x_t) - \frac{g}{g_s} \left( \tilde{C}_{uG} E_8^{uG}(x_t) + \tilde{C}_{uG}^* F_8^{uG}(x_t) \right) \right] \\ + \gamma_a \cdot \left( \tilde{C}_{\varphi q}^+ E_8^{\varphi q} + C_{\varphi q}^{(3)} F_8^{\varphi q} \right) + (1 + \gamma_a) \cdot \tilde{C}_{\varphi q}^{(3)} E_0'(x_t), \quad (51)$$

$$\Delta C_9^{\text{loop}} = \sqrt{2} \frac{m_t}{m_W} \left[ \left( \frac{Y_{uW}(x_t)}{\sin^2 \theta_w} - Z_{uW}(x_t) \right) \text{Re}(\tilde{C}_{uW}) - \frac{\cos \theta_w}{\sin \theta_w} Z_{uB}(x_t) \text{Re}(\tilde{C}_{uB}) \right] \\ + \frac{1}{\sin^2 \theta_w} \left[ (1 + \gamma_a) \cdot \left\{ -I_1(x_t) \left( \tilde{C}_{qe} + \tilde{C}_{lq}^{(1)} \right) + (1 - 4 \sin^2 \theta_w) \tilde{C}_{\varphi q}^{(1)} \right. \right. \\ \left. \left. + I_1^{lq(3)}(x_t) \tilde{C}_{lq}^{(3)} + \left( I_1^{\varphi q(3)}(x_t) + \sin^2 \theta_w I_2^{\varphi q(3)}(x_t) \right) \tilde{C}_{\varphi q}^{(3)} \right\} \right. \\ \left. + (1 + \gamma_b) \cdot I_1(x_t) \left( \tilde{C}_{eu} + \tilde{C}_{lu} + (-1 + 4 \sin^2 \theta_w) \tilde{C}_{\varphi u} \right) \right], \quad (52)$$

$$\Delta C_{10}^{\text{loop}} = -\frac{\sqrt{2}}{\sin^2 \theta_w} \frac{m_t}{m_W} Y_{uW}(x_t) \text{Re}(\tilde{C}_{uW}) + \frac{1}{\sin^2 \theta_w} \left[ (1 + \gamma_a) \cdot \left\{ I_1(x_t) \left( \tilde{C}_{lq}^{(1)} - \tilde{C}_{qe} - \tilde{C}_{\varphi q}^{(1)} \right) \right. \right. \\ \left. \left. - I_1^{lq(3)}(x_t) \tilde{C}_{lq}^{(3)} - \left( I_1^{\varphi q(3)}(x_t) + \sin^2 \theta_w I_2^{\varphi q(3)}(x_t) \right) \tilde{C}_{\varphi q}^{(3)} \right\} \right. \\ \left. + (1 + \gamma_b) \cdot I_1(x_t) \left( \tilde{C}_{eu} - \tilde{C}_{lu} + \tilde{C}_{\varphi u} \right) \right], \quad (53)$$

$$\Delta C_L^{\text{loop}} = \sqrt{2} \frac{m_t}{m_W} \frac{1}{\sin^2 \theta_w} I_{uW}^{\nu\bar{\nu}} \tilde{C}_{uW} + \frac{1}{\sin^2 \theta_w} \left[ (1 + \gamma_a) \cdot \left\{ I_1(x_t) \left( \tilde{C}_{lq}^{(1)} + \tilde{C}_{\varphi q}^{(1)} \right) \right. \right. \\ \left. \left. + I_{lq}^{\nu\bar{\nu}}(x_t) \tilde{C}_{lq}^{(3)} + I_{\varphi q}^{\nu\bar{\nu}}(x_t) \tilde{C}_{\varphi q}^{(3)} \right\} + (1 + \gamma_b) \cdot I_1(x_t) \left( -\tilde{C}_{lu} - \tilde{C}_{\varphi u} \right) \right], \quad (54)$$

$$\Delta C_{V,LL}^{\text{mix loop}} = \sqrt{2} \frac{m_t}{m_W} I_{uW}^{\text{mix}} \tilde{C}_{uW} + (1 + \gamma_a) \cdot \left( 32 \cdot I_1(x_t) \tilde{C}_{\varphi q}^{(1)} + (I_{\varphi q}^{\text{mix}} - 16 S_0(x_t)) \tilde{C}_{\varphi q}^{(3)} \right). \quad (55)$$

Note that the one-loop matching of  $\tilde{C}_{lq}^{(1)}$ ,  $\tilde{C}_{lq}^{(3)}$ ,  $\tilde{C}_{\varphi q}^{(3)}$  and  $\tilde{C}_{qe}$  onto  $C_9$  as well as  $C_{10}$  have been corrected with regard to Ref. [13]. We further only consider the leading contributions to  $C_{V,LL}^{\text{mix}}$  with regard to CKM suppression.

The one loop functions for the matching of the dipole operators read [101]:

$$E_7^{uW}(x_t) = \frac{-9x_t^3 + 63x_t^2 - 61x_t + 19}{48(x_t - 1)^3} + \frac{(3x_t^4 - 12x_t^3 - 9x_t^2 + 20x_t - 8) \ln(x_t)}{24(x_t - 1)^4} \\ + \frac{1}{8} \ln \left( \frac{m_W^2}{\mu_W^2} \right), \quad (56)$$

$$F_7^{uW}(x_t) = \frac{x_t(2 - 3x_t) \ln(x_t)}{4(x_t - 1)^4} - \frac{3x_t^3 - 17x_t^2 + 4x_t + 4}{24(x_t - 1)^3}, \quad (57)$$

$$E_7^{uB}(x_t) = -\frac{1}{8} \ln \left( \frac{m_W^2}{\mu_W^2} \right) - \frac{(x_t + 1)^2}{16(x_t - 1)^2} - \frac{x_t^2(x_t - 3) \ln(x_t)}{8(x_t - 1)^3}, \quad F_7^{uB}(x_t) = -\frac{1}{8}, \quad (58)$$

$$E_8^{uW}(x_t) = \frac{3x_t^2 - 13x_t + 4}{8(x_t - 1)^3} + \frac{(5x_t - 2) \ln(x_t)}{4(x_t - 1)^4}, \quad (59)$$

$$F_8^{uW}(x_t) = \frac{x_t^2 - 5x_t - 2}{8(x_t - 1)^3} + \frac{3x_t \ln(x_t)}{4(x_t - 1)^4}, \quad (60)$$

$$E_8^{uG}(x_t) = E_7^{uB}(x_t), \quad F_8^{uG}(x_t) = F_7^{uB}(x_t) \quad (61)$$

$$Y_{uW}(x_t) = \frac{3x_t}{4(x_t - 1)} - \frac{3x_t}{4(x_t - 1)^2} \ln(x_t), \quad (62)$$

$$Z_{uW}(x_t) = \frac{99x_t^3 - 136x_t^2 - 25x_t + 50}{36(x_t - 1)^3} - \frac{24x_t^3 - 45x_t^2 + 17x_t + 2}{6(x_t - 1)^4} \ln(x_t), \quad (63)$$

$$Z_{uB}(x_t) = -\frac{x_t^2 + 3x_t - 2}{4(x_t - 1)^2} + \frac{3x_t - 2}{2(x_t - 1)^3} \ln(x_t). \quad (64)$$

The loop functions for the matching of the vertex correcting penguin operators read [31]:

$$D'_0(x_t) = -\frac{8x_t^3 + 5x_t^2 - 7x_t}{12(x_t - 1)^3} + \frac{x_t^2(3x_t - 2)}{2(1 - x_t)^4} \ln(x_t), \quad (65)$$

$$E'_0(x_t) = -\frac{x_t(x_t^2 - 5x_t - 2)}{4(x_t - 1)^3} - \frac{3}{2} \frac{x_t^2}{(x_t - 1)^4} \ln(x_t), \quad (66)$$

$$E_7^{\varphi q}(x_t) = -\frac{1}{27}(2 \cos^2 \theta_w + 1), \quad F_7^{\varphi q}(x_t) = \frac{23}{18}, \quad (67)$$

$$E_8^{\varphi q}(x_t) = \frac{1}{9}(2 \cos^2 \theta_w + 1), \quad F_8^{\varphi q}(x_t) = \frac{2}{3}. \quad (68)$$

Note that we correct the overall and relative signs in comparison to [13]. We agree with the matching in [103] and extend it by higher orders in the MFV expansion. The loop functions for the matching of the four-fermion operators onto  $C_9, C_{10}$  read [101],[31] :

$$I_1(x_t) = -\frac{x_t}{16} \left[ \frac{x_t - 7}{2(x_t - 1)} + \ln(x_t) \frac{x_t^2 - 2x_t + 4}{(x_t - 1)^2} \right], \quad (69)$$

$$I^{lq^3}(x_t) = \frac{x_t}{16} \left[ \frac{-7x_t + 1}{2(x_t - 1)} + \ln(x_t) \frac{x_t^2 - 2x_t + 4}{(x_t - 1)^2} \right], \quad (70)$$

$$I_1^{\varphi q^3}(x_t) = \frac{x_t}{16} \left[ \frac{x_t + 17}{2(x_t - 1)} - \ln(x_t) \frac{7x_t^2 - 2x_t + 4}{(x_t - 1)^2} \right], \quad (71)$$

$$I_2^{\varphi q^3}(x_t) = \frac{x_t}{8} \left[ \frac{9x_t^3 + 355x_t^2 - 685x_t + 297}{2(x_t - 1)^2} - \ln(x_t) \frac{63x_t^5 - 156x_t^4 + 327x_t^3 - 450x_t^2 + 236x_t - 32}{(x_t - 1)^2} \right], \quad (72)$$

where the loop functions  $I^{lq^3}(x_t)$ ,  $I_1^{\varphi q^3}(x_t)$  and  $I_2^{\varphi q^3}(x_t)$  are corrected w.r.t. [13]. The loop functions for matching onto  $C_{V,LL}^{\text{mix}}$  read [31, 102]:

$$I_{uW}^{\text{mix}}(x_t) = -12x_t \left[ \frac{x_t + 1}{(x_t - 1)^2} - \ln(x_t) \frac{2x_t}{(x_t - 1)^3} \right], \quad (73)$$

$$I_{\varphi q}^{\text{mix}}(x_t) = x_t \left[ \frac{7x_t - 25}{(x_t - 1)} - \ln(x_t) \frac{2(x_t^2 - 14x_t + 4)}{(x_t - 1)^2} \right], \quad (74)$$

$$S_0(x_t) = \frac{x_t}{2} \left[ \frac{4 - 11x_t + x_t^2}{2(x_t - 1)^2} + \ln(x_t) \frac{3x_t^2}{(x_t - 1)^3} \right]. \quad (75)$$

The loop functions for the matching of the dineutrino Wilson coefficient  $C_L$  read:

$$I_{uw}^{\nu\bar{\nu}}(x_t) = \frac{3x_t - 6}{4(x_t - 1)} + \ln(x_t) \frac{3x_t}{4(x_t - 1)^2}, \quad (76)$$

$$I_{\varphi q}^{\nu\bar{\nu}}(x_t) = \frac{x_t}{16} \left[ \frac{x_t - 31}{2(x_t - 1)} + \ln(x_t) \frac{7x_t^2 - 2x_t - 20}{(x_t - 1)^2} \right], \quad (77)$$

$$I_{lq}^{\nu\bar{\nu}}(x_t) = -\frac{x_t}{16} \left[ \frac{7x_t - 1}{2(x_t - 1)} - \ln(x_t) \frac{x_t^2 - 26x_t + 28}{(x_t - 1)^2} \right]. \quad (78)$$

## B. Numerical Matching

The numerical matching conditions at the scale  $\mu = m_W$  read:

$$C_7 = -2.351 \tilde{C}_{uB} + 0.093 \tilde{C}_{uW} + \gamma_a \cdot \left( -0.095 \tilde{C}_{\varphi q}^+ + 1.278 \tilde{C}_{\varphi q}^{(3)} \right) \\ + (1 + \gamma_a) \cdot \left( -0.388 \tilde{C}_{\varphi q}^{(3)} \right), \quad (79)$$

$$C_8 = -0.664 \tilde{C}_{uG} + 0.271 \tilde{C}_{uW} + \gamma_a \cdot \left( 0.284 \tilde{C}_{\varphi q}^+ + 0.667 \tilde{C}_{\varphi q}^{(3)} \right) \\ + (1 + \gamma_a) \cdot \left( -0.194 \tilde{C}_{\varphi q}^{(3)} \right), \quad (80)$$

$$C_9 = 2.506 \tilde{C}_{uB} + 2.137 \tilde{C}_{uW} + \gamma_a \cdot \left( 430.511 \left( \tilde{C}_{qe} + \tilde{C}_{lq}^+ \right) - 45.858 \tilde{C}_{\varphi q}^+ \right) \\ + (1 + \gamma_a) \cdot \left( -0.213 \tilde{C}_{\varphi q}^{(1)} + 4.374 \tilde{C}_{\varphi q}^{(3)} + 2.003 \left( \tilde{C}_{qe} + \tilde{C}_{lq}^{(1)} \right) - 3.163 \tilde{C}_{lq}^{(3)} \right) \\ + (1 + \gamma_b) \left( 0.213 \tilde{C}_{\varphi u} + 2.003 \left( -\tilde{C}_{lu} - \tilde{C}_{eu} \right) \right), \quad (81)$$

$$C_{10} = -7.515 \tilde{C}_{uW} + \gamma_a \cdot 430.511 \left( \tilde{C}_{\varphi q}^+ + \tilde{C}_{qe} - \tilde{C}_{lq}^+ \right) \\ + (1 + \gamma_a) \cdot \left( 2.003 \left( \tilde{C}_{\varphi q}^{(1)} + \tilde{C}_{qe} - \tilde{C}_{lq}^{(1)} \right) - 17.884 \tilde{C}_{\varphi q}^{(3)} + 3.163 \tilde{C}_{lq}^{(3)} \right) \\ + (1 + \gamma_b) \cdot \left( 2.003 \left( -\tilde{C}_{\varphi u} - \tilde{C}_{eu} + \tilde{C}_{lu} \right) \right), \quad (82)$$

$$C_L = 12.889 \tilde{C}_{uW} + \gamma_a \cdot 430.511 \left( \tilde{C}_{\varphi q}^+ + \tilde{C}_{lq}^- \right) \\ + (1 + \gamma_a) \cdot \left( 2.003 \left( \tilde{C}_{\varphi q}^{(1)} + \tilde{C}_{lq}^{(1)} \right) - 22.830 \tilde{C}_{\varphi q}^{(3)} - 16.275 \tilde{C}_{lq}^{(3)} \right) \\ + (1 + \gamma_b) \cdot 2.003 \left( -\tilde{C}_{\varphi u} - \tilde{C}_{lu} \right), \quad (83)$$

$$C_{V,LL}^{\text{mix}} = -22.023 \tilde{C}_{uW} + \gamma_a \cdot \left( 14.317 \tilde{C}_{\varphi q}^{(1)} + 11.395 \tilde{C}_{\varphi q}^{(3)} \right). \quad (84)$$

## C. Fit results of Drell-Yan measurements

The individual limits for initial state quark-flavor compositions are given in Tab. VIII for the  $e^+e^-$  channel, in Tab. IX for the  $\mu^+\mu^-$  channel, in Tab. X for the  $\tau^+\tau^-$  channel and in Tab. XI

for the CC processes. We furthermore give the bounds on the FCNC quark-flavor combinations in Tab. XII.

Flavor	$\tilde{C}_{\varphi q}^{-/+}$	$\tilde{C}_{\varphi u/d}$	$\tilde{C}_{lu/d}$	$\tilde{C}_{eu/d}$	$\tilde{C}_{qe}$	$\tilde{C}_{lq}^{-/+}$
uu	[-0.085, 0.66]	[-0.24, 0.46]	[-0.0026, 0.0024]	[-0.0025, 0.0022]	[-0.0033, 0.0022]	[-0.002, 0.0017]
cc	[-0.11, 1.27]	[-1.03, 0.37]	[-0.018, 0.022]	[-0.014, 0.023]	[-0.020, 0.019]	[-0.0224, 0.0132]
dd	[-1.75, -0.02]	$\begin{bmatrix} -0.71, 0.6 \\ 0.84, 0.98 \end{bmatrix}$	[-0.0034, 0.0037]	[-0.0034, 0.0040]	[-0.0016, 0.0065]	[-0.0023, 0.0044]
ss	[-1.27, 0.05]	[-0.57, 0.84]	[-0.0162, 0.0142]	[-0.0176, 0.013]	[-0.0138, 0.0168]	[-0.0186, 0.0114]
bb	[-0.7, 0.14]	[-0.72, 0.98]	[-0.0315, 0.0285]	[-0.034, 0.028]	[-0.0142, 0.016]	[-0.0168, 0.0142]

TABLE VIII: 90% credible intervals of the flavor-specific quark-flavor diagonal NC DY fit of the  $pp \rightarrow e^+e^-$  observables considering only one quark-flavor combination in each fit, for  $\Lambda = 10$  TeV.

Flavor	$\tilde{C}_{\varphi q}^{-/+}$	$\tilde{C}_{\varphi u/d}$	$\tilde{C}_{lu/d}$	$\tilde{C}_{eu/d}$	$\tilde{C}_{qe}$	$\tilde{C}_{lq}^{-/+}$
uu	[-0.33, 1.19]	[-0.71, 0.60]	[-0.0018, 0.0022]	[-0.0018, 0.0027]	[-0.0032, 0.0022]	[-0.0013, 0.0022]
cc	[-0.36, 2.12]	[-1.94, 0.60]	[-0.009, 0.013]	[-0.007, 0.014]	[-0.0124, 0.0098]	[-0.0096, 0.0104]
dd	[-2.16, 0.17]	[-0.74, 1.41]	[-0.003, 0.0019]	[-0.0044, 0.002]	[-0.001, 0.006]	[-0.0027, 0.0027]
ss	[-2.08, 0.26]	[-0.78, 1.58]	[-0.0096, 0.0076]	[-0.0114, 0.0068]	[-0.0064, 0.0118]	[-0.0104, 0.007]
bb	[-1.18, 0.41]	[-1.30, 1.88]	[-0.018, 0.016]	[-0.0195, 0.0155]	[-0.0076, 0.0096]	[-0.0090, 0.0082]

TABLE IX: 90% credible intervals of the flavor-specific quark-flavor diagonal NC DY fit of the  $pp \rightarrow \mu^+\mu^-$  observables considering only one quark-flavor combination in each fit, for  $\Lambda = 10$  TeV.

Flavor	$\tilde{C}_{\varphi q}^{-/+}$	$\tilde{C}_{\varphi u/d}$	$\tilde{C}_{lu/d}$	$\tilde{C}_{eu/d}$	$\tilde{C}_{qe}$	$\tilde{C}_{lq}^{-/+}$
uu	[-0.22, 0.46]	[-0.46, 0.45]	[-0.0044, 0.0065]	[-0.0023, 0.0078]	[-0.0051, 0.006]	[-0.0020, 0.0073]
cc	[-0.42, 1.54]	[-1.28, 0.72]	[-0.023, 0.0245]	[-0.019, 0.027]	[-0.024, 0.023]	[-0.023, 0.021]
dd	[-0.66, 0.14]	[-0.83, 0.97]	[-0.0065, 0.0063]	[-0.0086, 0.0046]	[-0.0051, 0.0077]	[-0.0103, 0.0023]
ss	[-1.96, 0.24]	[-0.96, 1.26]	[-0.019, 0.019]	[-0.020, 0.019]	[-0.018, 0.021]	[-0.02, 0.02]
bb	[-0.95, 0.38]	[-1.18, 1.44]	[-0.038, 0.036]	[-0.044, 0.03]	[-0.018, 0.020]	[-0.020, 0.018]

TABLE X: 90% credible intervals of the flavor-specific quark-flavor diagonal NC DY fit of the  $pp \rightarrow \tau^+\tau^-$  observables considering only one quark-flavor combination in each fit, for  $\Lambda = 10$  TeV.

#### D. $B \rightarrow K$ Form Factors

We perform a fit of the form factors  $f_+$ ,  $f_0$  and  $f_T$  using a  $z$ -expansion to extrapolate the data from Lattice QCD (LQCD) as well as Light-Cone Sum Rules (LCSRs). We employ the BSZ

Flavor	$e\nu$		$\mu\nu$		$\tau\nu$	
	$\tilde{C}_{\varphi q}^{(3)}$	$\tilde{C}_{lq}^{(3)}$	$\tilde{C}_{\varphi q}^{(3)}$	$\tilde{C}_{lq}^{(3)}$	$\tilde{C}_{\varphi q}^{(3)}$	$\tilde{C}_{lq}^{(3)}$
ud	[-0.0085, 0.022]	[-0.0005, 0.0]	[-0.0142, 0.0064]	[-0.0001, 0.0003]	[-0.085, 0.255]	[-0.0018, 0.0002]
us	[-2.62, -1.42] [-0.72, 0.4]	[0.0013, -0.0111]	[-2.4, -1.58] [-0.6, 0.3]	[-0.0126, 0.005]	[-2.14, 1.16]	[-0.0108, 0.0043]
ub	[-61, 60]	[-0.36, 0.37]	[-48, 47]	[-0.56, 0.56]	[-168, 172]	[-0.71, 0.7]
cd	[-2.36, 0.42]	[-0.012, 0.0036]	[-2.34, 0.3]	[-0.0164, 0.0076]	[-4.45, 2.35]	[-0.0192, 0.0088]
cs	[-0.12, 0.13]	[-0.005, 0.0023]	[-0.098, 0.11]	[-0.0082, 0.0038]	[-2.9, 0.75]	[-0.0138, 0.003]
cb	[-11.6, 9.6]	[-0.136, 0.13]	[-10, 8]	[-0.23, 0.215]	[-47, 45]	[-0.24, 0.24]

TABLE XI: 90% credible limits of the flavor-specific CC DY fits considering only one quark-flavor combination in each fit. The fits are performed assuming  $\Lambda = 10$  TeV.

Flavor	$ee$			$\mu\mu$		
	$\tilde{C}_{\varphi q}^{(+)}$	$\tilde{C}_{qe}$	$\tilde{C}_{lq}^{(+)}$	$\tilde{C}_{\varphi q}^{(+)}$	$\tilde{C}_{qe}$	$\tilde{C}_{lq}^{(+)}$
ds	[-750, 740]	[-13.8, 13.8]	[-14.2, 13.8]	[-1440, 1440]	[-9, 9]	[-8.8, 8.6]
db	[-35.5, 35.5]	[-0.76, 0.77]	[-0.76, 0.78]	[-70, 70]	[-0.47, 0.49]	[-0.47, 0.46]
sb	[-11.2, 11.2]	[-0.44, 0.44]	[-0.44, 0.45]	[-24.5, 24.5]	[-0.265, 0.265]	[-0.26, 0.265]

Flavor	$\tau\tau$		
	$\tilde{C}_{\varphi q}^{(+)}$	$\tilde{C}_{qe}$	$\tilde{C}_{lq}^{(+)}$
ds	[-1220, 1180]	[-20, 20.5]	[-21, 20.5]
db	[-60, 60]	[-0.94, 0.94]	[-0.96, 0.94]
sb	[-18, 18]	[-0.49, 0.49]	[-0.5, 0.5]

TABLE XII: 90% credible limits of the FCNC flavor combinations of the DY fit considering only one quark-flavor combination in each fit. Shown are the results of the  $pp \rightarrow e^+e^-$  fit (upper left), the  $pp \rightarrow \mu^+\mu^-$  fit (upper right) and the  $pp \rightarrow \tau^+\tau^-$  fit (lower center). The fits are performed assuming  $\Lambda = 10$  TeV.

parameterization [104]

$$f_i(q^2) = \frac{1}{P_i(q^2)} \sum_{n=0}^{K-1} a_n^i [z(q^2) - z(0)]^n, \quad (85)$$

with the pole factors

$$P_i(q^2) = 1 - q^2/M_{B_i}^2, \quad (86)$$

the pole masses  $M_{B_i} = M_{B_s^*}$  for  $f_{+,T}$  and  $M_{B_i} = M_{B_s^0}$  for  $f_0$ , and the conformal mapping

$$z(q^2) = \frac{\sqrt{t_+ - q^2} - \sqrt{t_+ - t_0}}{\sqrt{t_+ - q^2} + \sqrt{t_+ - t_0}}, \quad (87)$$

where  $t_+ = (M_{B^+} + M_{K^+})^2$ . We chose  $t_0 = (M_{B^+} + M_{K^+})(\sqrt{M_{B^+}} - \sqrt{M_{K^+}})^2$ , which maps the physically allowed values of  $q^2$  onto the region with  $|z| < 0.15$ . As numerical inputs, we use  $M_{B_s^*} = 5.4154$  GeV [105] and  $M_{B^0} = 5.711$  GeV [106].

We use  $K = 3$ , resulting in three parameters  $a_n^i$  per form factor. Eq. (85) implies  $f_i(0) = a_0^i$ , hence the consistency relation  $f_+(0) = f_0(0)$  can be implemented in a straightforward way by using a common parameter  $a_0^{+/0} = a_0^+ = a_0^0$ .

We fit the latest lattice LQCD results from the HPQCD collaboration [107] together with results from LCSRs [66]. As LQCD is most precise for high values of  $q^2$ , we include synthetic data generated at  $q^2 \in (18, 20, 22)$  GeV<sup>2</sup>. LCSRs are, in contrast, only valid for low  $q^2$ , so that we include LCSR data for  $q^2 \in (-15, -10, -5)$  GeV<sup>2</sup>. The resulting parameters  $a_n^i$  together with the uncertainties and the correlation matrix are given in Tab. XIII. We furthermore illustrate the results in Fig. 13 as a function of  $q^2$  and compare it to other recent fit results [66, 108]. We find that our results are consistent with the literature and that the uncertainties are significantly reduced due to the recent HPQCD results.

$a_0^{+/0}$	$a_1^+$	$a_2^+$	$a_1^0$	$a_2^0$	$a_0^T$	$a_1^T$	$a_2^T$
0.3233(67)	-0.966(64)	0.12(11)	0.214(57)	-0.12(13)	0.3177(95)	-0.999(86)	0.17(35)
1	0.4784	0.1622	0.8083	0.5481	0.5610	0.2543	0.0015
	1	0.5721	0.5357	0.4012	0.2953	0.2599	0.0409
		1	0.2224	0.2191	0.1077	0.1231	0.0439
			1	0.9074	0.471	0.2604	0.0239
				1	0.3268	0.1902	0.0459
					1	-0.129	-0.4515
						1	0.646
							1

TABLE XIII: Fit results and correlation matrix of the  $z$ -expansion coefficients. We employ the BSZ parameterization in Eq. (85) with  $K = 3$  and consider data from LCSRs [66] as well as the latest LQCD results from the HPQCD collaboration [107].



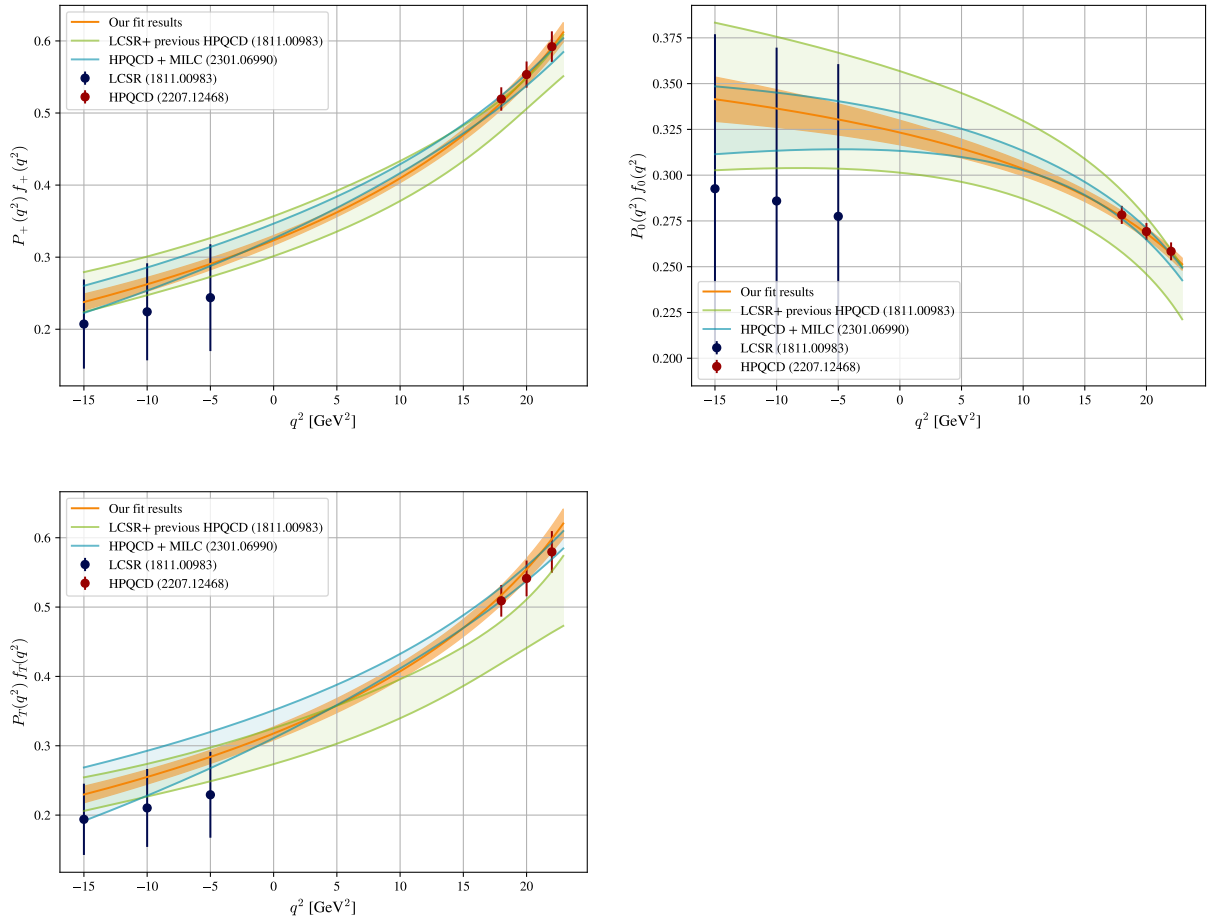


FIG. 13: Results of our form factor expansion multiplied by the corresponding pole factors together with the data employed for the fit [66, 107]. We compare our results to the  $z$ -expansion fit with LCSR data and the previous HPQCD results [66, 109], as well as to the results using LQCD results only [108].

- 
- [1] J. Drobnak, S. Fajfer, and J. F. Kamenik, Phys. Lett. B **701**, 234 (2011), 1102.4347.
  - [2] J. Drobnak, S. Fajfer, and J. F. Kamenik, Nucl. Phys. B **855**, 82 (2012), 1109.2357.
  - [3] H. Gong, Y.-D. Yang, and X.-B. Yuan, JHEP **05**, 062 (2013), 1301.7535.
  - [4] S. Bifmann, J. Erdmann, C. Grunwald, G. Hiller, and K. Kröninger, Eur. Phys. J. C **80**, 136 (2020), 1909.13632.
  - [5] X.-Q. Li, Y.-D. Yang, and X.-B. Yuan, JHEP **03**, 018 (2012), 1112.2674.
  - [6] J. Brod, A. Greljo, E. Stamou, and P. Uttayarat, JHEP **02**, 141 (2015), 1408.0792.
  - [7] R. Bause, H. Gisbert, M. Golz, and G. Hiller, Eur. Phys. J. C **82**, 164 (2022), 2007.05001.
  - [8] B. Grzadkowski, M. Iskrzynski, M. Misiak, and J. Rosiek, JHEP **10**, 085 (2010), 1008.4884.

- [9] G. D'Ambrosio, G. F. Giudice, G. Isidori, and A. Strumia, Nucl. Phys. B **645**, 155 (2002), hep-ph/0207036.
- [10] S. Bruggisser, R. Schäfer, D. van Dyk, and S. Westhoff, JHEP **05**, 257 (2021), 2101.07273.
- [11] R. Aoude, T. Hurth, S. Renner, and W. Shepherd, JHEP **12**, 113 (2020), 2003.05432.
- [12] S. Bruggisser, D. van Dyk, and S. Westhoff (2022), 2212.02532.
- [13] S. Bißmann, C. Grunwald, G. Hiller, and K. Kröninger, JHEP **06**, 010 (2021), 2012.10456.
- [14] D. Barducci et al. (2018), 1802.07237.
- [15] R. Barbieri, D. Buttazzo, F. Sala, and D. M. Straub, JHEP **07**, 181 (2012), 1203.4218.
- [16] D. A. Faroughy, G. Isidori, F. Wilsch, and K. Yamamoto, JHEP **08**, 166 (2020), 2005.05366.
- [17] A. Greljo, A. Palavrić, and A. E. Thomsen, JHEP **10**, 010 (2022), 2203.09561.
- [18] A. Efrati, A. Falkowski, and Y. Soreq, JHEP **07**, 018 (2015), 1503.07872.
- [19] A. Greljo and D. Marzocca, Eur. Phys. J. C **77**, 548 (2017), 1704.09015.
- [20] J. Fuentes-Martin, A. Greljo, J. Martin Camalich, and J. D. Ruiz-Alvarez, JHEP **11**, 080 (2020), 2003.12421.
- [21] A. Angelescu, D. A. Faroughy, and O. Sumensari, Eur. Phys. J. C **80**, 641 (2020), 2002.05684.
- [22] L. Allwicher, D. A. Faroughy, F. Jaffredo, O. Sumensari, and F. Wilsch (2022), 2207.10714.
- [23] W. Buchmuller and D. Wyler, Nucl. Phys. B **268**, 621 (1986).
- [24] A. Kobach, Phys. Lett. B **758**, 455 (2016), 1604.05726.
- [25] I. Brivio, JHEP **04**, 073 (2021), 2012.11343.
- [26] E. E. Jenkins, A. V. Manohar, and M. Trott, JHEP **10**, 087 (2013), 1308.2627.
- [27] E. E. Jenkins, A. V. Manohar, and M. Trott, JHEP **01**, 035 (2014), 1310.4838.
- [28] R. Alonso, E. E. Jenkins, A. V. Manohar, and M. Trott, JHEP **04**, 159 (2014), 1312.2014.
- [29] J. Aebischer, J. Kumar, and D. M. Straub, Eur. Phys. J. C **78**, 1026 (2018), 1804.05033.
- [30] P. Paradisi, M. Ratz, R. Schieren, and C. Simonetto, Phys. Lett. B **668**, 202 (2008), 0805.3989.
- [31] W. Dekens and P. Stoffer, JHEP **10**, 197 (2019), 1908.05295.
- [32] G. Colangelo, E. Nikolidakis, and C. Smith, Eur. Phys. J. C **59**, 75 (2009), 0807.0801.
- [33] C. Hays, A. Martin, V. Sanz, and J. Setford, JHEP **02**, 123 (2019), 1808.00442.
- [34] S. Dawson, S. Homiller, and M. Sullivan, Phys. Rev. D **104**, 115013 (2021), 2110.06929.
- [35] T. Corbett, A. Helset, A. Martin, and M. Trott, JHEP **06**, 076 (2021), 2102.02819.
- [36] R. Boughezal, E. Mereghetti, and F. Petriello, Phys. Rev. D **104**, 095022 (2021), 2106.05337.
- [37] R. Boughezal, Y. Huang, and F. Petriello, Phys. Rev. D **106**, 036020 (2022), 2207.01703.
- [38] S. Bißmann, J. Erdmann, C. Grunwald, G. Hiller, and K. Kröninger, Phys. Rev. D **102**, 115019 (2020), 1912.06090.
- [39] J. Alwall, R. Frederix, S. Frixione, V. Hirschi, F. Maltoni, O. Mattelaer, H. S. Shao, T. Stelzer, P. Torrielli, and M. Zaro, JHEP **07**, 079 (2014), 1405.0301.
- [40] R. Frederix, S. Frixione, V. Hirschi, D. Pagani, H. S. Shao, and M. Zaro, JHEP **07**, 185 (2018), [Erratum: JHEP 11, 085 (2021)], 1804.10017.

- [41] R. D. Ball et al., Nucl. Phys. B **867**, 244 (2013), 1207.1303.
- [42] A. Buckley, J. Ferrando, S. Lloyd, K. Nordström, B. Page, M. Rüfenacht, M. Schönherr, and G. Watt, Eur. Phys. J. C **75**, 132 (2015), 1412.7420.
- [43] I. Brivio, Y. Jiang, and M. Trott, JHEP **12**, 070 (2017), 1709.06492.
- [44] A. Tumasyan et al. (CMS), Phys. Rev. D **104**, 092013 (2021), 2108.02803.
- [45] A. Kulesza et al., Eur. Phys. J. C **79**, 249 (2019), 1812.08622.
- [46] G. Bevilacqua, H. B. Hartanto, M. Kraus, T. Weber, and M. Worek, JHEP **10**, 158 (2018), 1803.09916.
- [47] A. Kulesza et al., Eur. Phys. J. C **80**, 428 (2020), 2001.03031.
- [48] ATLAS Collaboration, ATLAS-CONF-2019-004 (2019).
- [49] A. Czarnecki, J. G. Korner, and J. H. Piclum, Phys. Rev. D **81**, 111503 (2010), 1005.2625.
- [50] A. M. Sirunyan et al. (CMS), JHEP **07**, 208 (2021), 2103.02708.
- [51] G. Aad et al. (ATLAS), Phys. Rev. Lett. **125**, 051801 (2020), 2002.12223.
- [52] G. Aad et al. (ATLAS), Phys. Rev. D **100**, 052013 (2019), 1906.05609.
- [53] ATLAS Collaboration, ATLAS-CONF-2021-025 (2021).
- [54] C. Zhang, Phys. Rev. D **90**, 014008 (2014), 1404.1264.
- [55] E. Conte, B. Fuks, and G. Serret, Comput. Phys. Commun. **184**, 222 (2013), 1206.1599.
- [56] G. Aad et al. (ATLAS), Eur. Phys. J. C **81**, 737 (2021), 2103.12603.
- [57] G. Aad et al. (ATLAS), JHEP **09**, 049 (2020), 2007.06946.
- [58] A. Tumasyan et al. (CMS), JHEP **07**, 219 (2023), 2208.06485.
- [59] G. Aad et al. (ATLAS), Phys. Lett. B **843**, 137829 (2023), 2209.14903.
- [60] C. Bierlich et al. (2022), 2203.11601.
- [61] J. de Favereau, C. Delaere, P. Demin, A. Giammanco, V. Lemaître, A. Mertens, and M. Selvaggi (DELPHES 3), JHEP **02**, 057 (2014), 1307.6346.
- [62] I. Antcheva et al., Comput. Phys. Commun. **180**, 2499 (2009), 1508.07749.
- [63] F. Krauss, S. Kuttimalai, and T. Plehn, Phys. Rev. D **95**, 035024 (2017), 1611.00767.
- [64] D. M. Straub (2018), 1810.08132.
- [65] S. Schael et al. (ALEPH, DELPHI, L3, OPAL, SLD, LEP Electroweak Working Group, SLD Electroweak Group, SLD Heavy Flavour Group), Phys. Rept. **427**, 257 (2006), hep-ex/0509008.
- [66] N. Gubernari, A. Kokulu, and D. van Dyk, JHEP **01**, 150 (2019), 1811.00983.
- [67] R. R. Horgan, Z. Liu, S. Meinel, and M. Wingate, PoS **LATTICE2014**, 372 (2015), 1501.00367.
- [68] A. Tumasyan et al. (CMS), Phys. Lett. B **842**, 137955 (2023), 2212.10311.
- [69] M. Beneke, C. Bobeth, and R. Szafron, JHEP **10**, 232 (2019), [Erratum: JHEP 11, 099 (2022)], 1908.07011.
- [70] R. Aaij et al. (LHCb), Phys. Rev. D **105**, 012010 (2022), 2108.09283.
- [71] Y. Amhis et al. (HFLAV) (2022), 2206.07501.
- [72] M. Misiak et al., Phys. Rev. Lett. **114**, 221801 (2015), 1503.01789.
- [73] J. P. Lees et al. (BaBar), Phys. Rev. Lett. **112**, 211802 (2014), 1312.5364.

- [74] Y. Sato et al. (Belle), Phys. Rev. D **93**, 032008 (2016), [Addendum: Phys.Rev.D 93, 059901 (2016)], 1402.7134.
- [75] T. Huber, T. Hurth, and E. Lunghi, JHEP **06**, 176 (2015), 1503.04849.
- [76] R. Aaij et al. (LHCb), Phys. Rev. Lett. **125**, 011802 (2020), 2003.04831.
- [77] R. Aaij et al. (LHCb), JHEP **06**, 133 (2014), 1403.8044.
- [78] R. Aaij et al. (LHCb), JHEP **11**, 043 (2021), 2107.13428.
- [79] R. Aaij et al. (LHCb), JHEP **06**, 115 (2015), [Erratum: JHEP 09, 145 (2018)], 1503.07138.
- [80] L. Di Luzio, M. Kirk, A. Lenz, and T. Rauh, JHEP **12**, 009 (2019), 1909.11087.
- [81] J. P. Lees et al. (BaBar), Phys. Rev. D **87**, 112005 (2013), 1303.7465.
- [82] J. Grygier et al. (Belle), Phys. Rev. D **96**, 091101 (2017), [Addendum: Phys.Rev.D 97, 099902 (2018)], 1702.03224.
- [83] G. Buchalla, G. Hiller, and G. Isidori, Phys. Rev. D **63**, 014015 (2000), hep-ph/0006136.
- [84] S. Aoki et al. (Flavour Lattice Averaging Group), Eur. Phys. J. C **80**, 113 (2020), 1902.08191.
- [85] J. Brod, M. Gorbahn, and E. Stamou, PoS **BEAUTY2020**, 056 (2021), 2105.02868.
- [86] J. F. Kamenik and C. Smith, Phys. Lett. B **680**, 471 (2009), 0908.1174.
- [87] W. Altmannshofer et al. (Belle-II), PTEP **2019**, 123C01 (2019), [Erratum: PTEP 2020, 029201 (2020)], 1808.10567.
- [88] N. Castro, J. Erdmann, C. Grunwald, K. Kröninger, and N.-A. Rosien, Eur. Phys. J. C **76**, 432 (2016), 1605.05585.
- [89] O. Schulz, F. Beaujean, A. Caldwell, C. Grunwald, V. Hafych, K. Kröninger, S. La Cagnina, L. Röhrig, and L. Shtembari (2020), 2008.03132.
- [90] A. Greljo, J. Salko, A. Smolkovič, and P. Stangl (2022), 2212.10497.
- [91] B. Yan and C. P. Yuan, Phys. Rev. Lett. **127**, 051801 (2021), 2101.06261.
- [92] R. Bause, H. Gisbert, M. Golz, and G. Hiller, JHEP **12**, 061 (2021), 2109.01675.
- [93] ATLAS Collaboration (2023), 2302.01283.
- [94] T. C. Collaboration et al. (CMS), JHEP **03**, 095 (2021), 2012.04120.
- [95] CMS Collaboration, CMS-PAS-TOP-22-006 (2023).
- [96] A. Abada et al. (FCC), Eur. Phys. J. ST **228**, 261 (2019).
- [97] K. Long, D. Lucchesi, M. Palmer, N. Pastrone, D. Schulte, and V. Shiltsev, Nature Phys. **17**, 289 (2021), 2007.15684.
- [98] C. Aime et al. (2022), 2203.07256.
- [99] R. Bause, H. Gisbert, M. Golz, and G. Hiller (2022), 2209.04457.
- [100] S. Glazov, for the Belle II collaboration, "Belle II Physics highlights", Talk given at EPS-HEP on August 24, 2023, Hamburg, Germany.
- [101] J. Aebischer, A. Crivellin, M. Fael, and C. Greub, JHEP **05**, 037 (2016), 1512.02830.
- [102] C. Bobeth, A. J. Buras, A. Celis, and M. Jung, JHEP **07**, 124 (2017), 1703.04753.
- [103] T. Hurth, S. Renner, and W. Shepherd, JHEP **06**, 029 (2019), 1903.00500.

- [104] A. Bharucha, D. M. Straub, and R. Zwicky, *JHEP* **08**, 098 (2016), 1503.05534.
- [105] R. L. Workman et al. (Particle Data Group), *PTEP* **2022**, 083C01 (2022).
- [106] C. B. Lang, D. Mohler, S. Prelovsek, and R. M. Woloshyn, *Phys. Lett. B* **750**, 17 (2015), 1501.01646.
- [107] W. G. Parrott, C. Bouchard, and C. T. H. Davies ((HPQCD collaboration)§, HPQCD), *Phys. Rev. D* **107**, 014510 (2023), 2207.12468.
- [108] D. Bečirević, G. Piazza, and O. Sumensari, *Eur. Phys. J. C* **83**, 252 (2023), 2301.06990.
- [109] C. Bouchard, G. P. Lepage, C. Monahan, H. Na, and J. Shigemitsu (HPQCD), *Phys. Rev. D* **88**, 054509 (2013), [Erratum: *Phys.Rev.D* 88, 079901 (2013)], 1306.2384.